OPTIMIZATION OF A 3-AXIS INDUCTION MAGNETOMETER FOR AIRBORNE GEOPHYSICAL EXPLORATION

by

J. Christian Dupuis

BScE, University of New Brunswick, 2001

A thesis submitted in partial fulfilment of the requirements for the degree of

Master of Science in Engineering

in the graduate academic unit of Electrical and Computer Engineering

Supervisor(s)	Dr. Bruce G. Colpitts, BScE, MScE, PhD (UNB)
	Dr. Brent R. Petersen, BEng (Carleton), MASc (Waterloo), PhD (Carleton)
Examining Board	Dr. Dennis F. Lovely, BSc (Southampton), PhD (Strathclyde)
	Prof. David McG. Luke, BScEng, MScEng (Natal)
External Examiner	Dr. Karl E. Butler, BSc (Queen's), MSc, PhD (UBC)

This thesis is accepted

Dean of Graduate Studies

UNIVERSITY OF NEW BRUNSWICK

Acknowledgments

I would like to take this time to express my gratitude to the following individuals and organizations who have made this project possible,

Dr. Bruce G. Colpitts and Dr. Brent R. Petersen for their help and guidance,

Darryl A. Curley and Custom Research Ltd. for allowing me to take part in their project, providing financial support, and supplying material for the construction of the prototypes,

National Science and Engineering Research Council for their financial support via an Industrial Postgraduate Scholarship,

Dr. Micheal L. Burrows for his insight in the construction of laminated mu-metal cores for induction magnetometers,

Dr. Adel M. Sharaf for providing me with the reference to the book by G. R. Slemon,

Dr. Dennis F. Lovely for his insight in noise calculations, and finally

my family and Michelle Watt for their support during this journey.

Abstract

The present work, develops a methodology to optimize the performance of conventional induction magnetometers (CIM) and develops a new concept in their implementation. From a logistic standpoint, the CIMs have to remain as small and light as possible. The use of permeable cores to concentrate the flux increases the apparent area and increases the sensitivity of the CIM. The dimensions of the permeable core affect the overall weight of the sensor and its performance. For permeable rod cores, the permeability is proportional of the length-to-diameter ratio. The novel idea developed in this work is to use an array of elemental induction magnetometers (EIM)s instead of a single CIM. The weight of the CIM is thus distributed amongst multiple EIMs and for the same weight there is substantial signal-to-noise ratio (SNR) improvements. There is also a decrease in the overall inductance which translates into greater bandwidths.

Contents

List of Figures

List of Variables

V ..... Induced voltage

Φ ..... Magnetic flux

t ..... Time

N ..... Number of turns

μ_{core} ..... Permeability of the core

μ_o ..... Permeability of free space

A ..... Cross-sectional area of the core

ω ..... Angular frequency

H_o ..... Magnetic field intensity

s_1 ..... Half length of winding

l_c ..... Half length of the core

r_c ..... Radius of the core

W_s ..... Total weight of induction magnetometer

W_c ..... Weight of the core

W_w ..... Weight of the winding

V_c ..... Volume of the core

A_r ..... Scaling factor to describe helix in $\vec{i}$

B_r ..... Scaling factor to describe helix in $\vec{j}$

C_r ..... Scaling factor to describe helix in $\vec{k}$

ρ_c ..... Density of the core

V_w ..... Volume of the winding

ρ_w ..... Density of the winding material

l_w ..... Half length of the wire

r_w ..... Radius of the wire

d_w ..... Diameter of the wire

N_{tl} ..... Number of turns per layer

N_t ..... Total number of turns

r_{av} ..... Average winding radius

N_s ..... Number of scramble turns

γ_f ..... Fill factor

r_{core} ..... Radius of the core

n_{layers} ..... Number of layers

N_{ll} ..... Number of turns on the last layer

R_w ..... Resistance of the winding

L ..... Inductance

C ..... Capacitance

R_c ..... Resistance equivalent to Eddy current core losses

c ..... Lamination thickness

A_c ..... Cross sectional area of the core

ρ ..... Resistivity of core material

l ..... Length of wire

A_w ..... Cross sectional area of the wire

ρ_{wire} ..... Resistivity of the wire

Q ..... Quality factor of a resonating circuit

h ..... Planck's constant

f ..... Center frequency

B ..... Noise bandwidth

R ..... Resistance

T ..... Temperature

k ..... Boltzmann's constant

v_n ..... Noise voltage

R_p ..... Parallel resistance

$E_w{}^2$ ..... Thermal noise due to winding resistance

$E_{tp}{}^2$ ..... Thermal noise due to parallel resistance

$E_n{}^2$ ..... Amplifier noise voltage

$E_{nf}{}^2$ ..... Thermal noise voltage of the feedback resistor

$I_n{}^2$ ..... Amplifier noise current

$I_{nf}{}^2$ ..... Noise current associated with feedback resistor

$I_{np}{}^2$ ..... Noise current associated to parallel resistance

$E_{no}{}^2$ ..... Equivalent output noise

$E_{ni}{}^2$ ..... Input refered noise

R_f ..... Feedback resistance

C_f ..... Feedback capacitance

n ..... Length-to-diameter ratio

Z_{TEM} ..... Impedance of a TEM line

List of Acronyms

CIM ..... Conventional Induction Magnetometer

EIM ..... Elemental Induction Magnetometer

ATEM ..... Airborne Transient Electromagnetic Method

FEM ..... Frequency Electromagnetic Method

TEM ..... Transient Electromagnetic Method

VLF ..... Very Low Frequency

ELF ..... Extremely Low Frequency

LORAN ..... LOng RAnge Navigation

INPUT ..... INduced PUlse Transient system

SQUID ..... Superconducting Quantum Interference Device

MAD ..... Magnetic Anomaly Detection

SNR ..... Signal-to-Noie Ratio

FD ..... Frequency Domain

TD ..... Time Domain

OIMA ..... Orthogonal Induction Magnetometer Array

SAIMA ..... Single Axis Induction Magnetometer

1 Introduction

The aim of this research is to develop magnetic sensors for the next generation of Airborne Transient ElectroMagnetic (ATEM) exploration systems designed by Custom Research Ltd. Conventional induction magnetometers (CIM) have long been the sensor of choice for electromagnetic exploration. Previous work was done by Breen and Becker [Breen64, Becker67] to develop models and methods for air cored CIMs for ground Frequency ElectroMagnetic (FEM) exploration methods. Most of this work does not apply to ATEM because as the reader will see in this thesis, there are significant differences between the requirements of ground FEM and ATEM. A large part of this document is aimed at providing a comprehensive design and optimization method for CIMs used in ATEM. CIMs form part of the competitive advantage of exploration companies and therefore cannot be purchased as off-the-shelf components. This means that every sensor system is unique to its exploration company. In this case, the bandwidth needed span from 20 Hz to 20 kHz. The receiver system is part of a larger system and therefore was confined to the weight and aerodynamic drag budget of the system. Figure 1 illustrates the basic setup of an ATEM system.

This document was written in order to be a good reference for the construction of CIMs. The first part of the document presents a brief overview of the electromagnetic methods used in geophysical exploration. The second part takes a closer look at the magnetic sensors available. The third part introduces the CIM and provides physical and electrical models. The fourth part takes a look at the noise sources present in electromagnetic geophysical exploration. The fifth part looks at the optimization of CIMs given the models developed previously. The concept of arrays of elemental induction magnetometers (EIM) is also introduced in this section. The last parts look at the construction and calibration of the

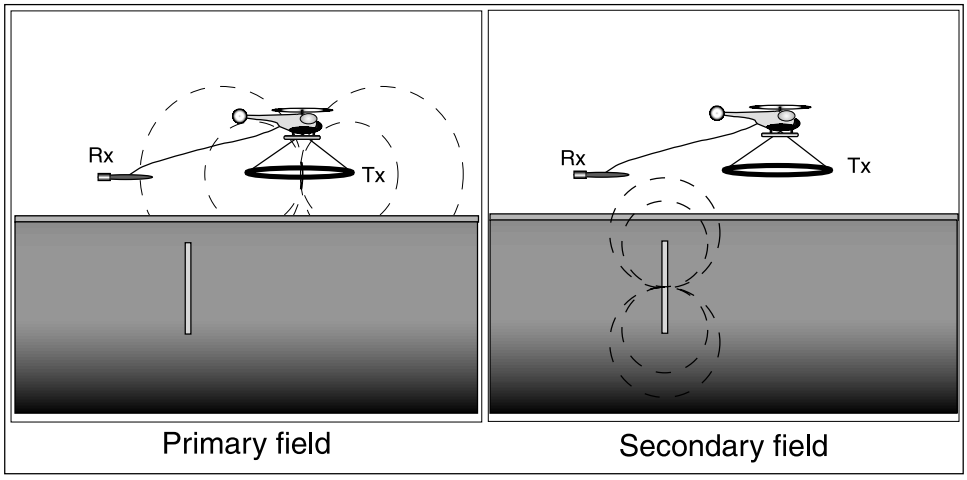

Figure 1: Basic ATEM system

sensor system developed and also at the validation of the models used. Finally, conclusions are drawn on the successful completion of this project and suggestions for future work are made.

2 Exploration Techniques

There exist many varied methods to find ore bodies in the ground. A good description of the most popular methods can be found in work by Parasnis [Parasnis97] and Telford *et al* [Telford90]. Each method makes use of physical attributes of the ore deposit and the medium which surrounds it. Although there are well over eleven methods covered in the work of Parasnis [Parasnis97] and Telford *et al* [Telford90], the only methods of interest in this thesis will be electromagnetic methods.

2.1 Ground Surveys

Most methods were first designed to work on the ground. These methods allow geophysicists and prospectors to survey small easily accessible areas. Unfortunately, most of the interesting survey sites are not always easily accessible by land. They may be in remote areas such as forests or deserts where no roads have been built. The logistical problems of getting a ground crew to the site is a small one in comparison to the hardship of making the actual survey. Getting a ground crew to explore any significant area in a timely and cost effective fashion can be a significant problem.

2.2 Airborne Surveys

The logical answer to the problems faced by ground crews is an airborne exploration system. Although the instrumentation tends to be more expensive, and the flight time makes up a considerable part of the expenses, it soon becomes a cost effective alternative if a sizable area must be explored. The complexity of the equipment and the logistics involved in the development of an ATEM system increase. Noise sources are introduced because of the movement of the system in space. Earlier systems also had lower resolution because surveys were carried out from fixed wing aircraft that had to fly at high altitude. New helicopter ATEM systems provide a lower noise platform which can be flown more slowly and at lower altitude and hence gather higher resolution data.

From all the methods available for geophysical exploration, only a handful can be transferred successfully to an airborne platform. Methods which have been implemented on board flying vehicles include gravity methods, magnetic methods, radioactivity methods and electromagnetic methods. All of these methods were initially developed to accomplish a similar task: to find a buried mineral or hydrocarbon deposit. In subsequent years however

application of airborne geophysical methods have expanded to include geologic mapping, ground water exploration, environmental monitoring, the detection of unexploded ordonance and other objectives. In general, the nature of the target will dictate which method will work the best. In the case of oil exploration, the gravity method's is usually more appropriate than the electromagnetic methods. This relates to the diagnostic properties of the exploration target and the required depth of exploration. Hydrocarbon reserves are sometimes associated with subsurface structures that have anomalous densities and therefore cause local variations in the earth's gravity field. In contrast, they are rarely associated with significant variations in conductivity that are close enough to surface to be detected by EM methods. Certain types of ore bodies however are highly conductive compared with their surroundings and are therefore well suited to detection by electromagnetic systems.

3 Basis of the Electromagnetic Methods

All of the EM methods are governed by *Faraday's law* of electromagnetic induction which states that:

> "The electromotive force induced in a stationary closed circuit is equal to the negative rate of increase of the magnetic flux linking the circuit"[Cheng89]

The sources used to establish the primary field in EM methods are of two different types. The first consist of a continuous sine wave while the second consists of a series of pulses. These two different sources form the basis of two different approach to EM exploration : Frequency Domain (FD) and Time Domain (TD) techniques. Both techniques are described below. These descriptions are based on the explanations given in the work by Parasnis [Parasnis97].

3.1 Frequency Domain

In this type of system, the transmitter emits a time varying sinusoidal field. This primary field induces eddy currents in a conductive target. These eddy currents generate a secondary field which tries to oppose the changes in the primary. The strength of the secondary and its phase relative to the primary are indicative of the quality of the conductor. Since the system for which the sensors will be built is a TD system, the FD systems will only be discussed in general terms. A more detailed discussion about the FD system can be found in work by Parasnis [Parasnis97], Telford *et al* [Telford90] and Nabighian [Nabighian88].

3.2 Time Domain Electromagnetic Methods

This technique relies on the law of induction stated in section 3. In this case, the primary field is generated by transient pulses. The signal of interest is produced when the transmitter makes the transition between the ON state to the OFF state. During this transition, the magnetic field that was applied to the conductor is changing with time and thus a current and a secondary field is created. For good conductors, where the resistance is low, the current will persist for a longer time and thus the secondary field will decay slowly. For poor conductors, where the resistance is high, the current will decrease rapidly and thus the secondary field will decay much faster. In order to illustrate this concept better, the following example adapted from work by Parasnis [Parasnis97] is presented.

The current in the ore body usually flows around its perimeter which forms closed contours. Although the shapes are generally irregular, we can get a basic understanding of the principles by considering a single loop of wire which, in electrical terms, has a resistance and an inductance. Imagine that this loop is placed under our exploration system. Summing the voltages around the loop in accordance with Kirchoff's Voltage Law will

yield

$$RI + L\frac{dI}{dt} = 0\,. \tag{1}$$

By inspection, the answer to this first order differential equation is given by

$$I = I_o\, e^{-\frac{R}{L}t}\,, \tag{2}$$

where I_o is the current immediately after the primary field is switched off. From the Biot-Savart law, we know that the magnetic field caused by a current around a closed path is proportional to the current and thus we can write the secondary field as

$$S = S_o\, e^{-\frac{R}{L}t}\,, \tag{3}$$

where S_o is the secondary field immediately after the primary field is switched off. This example shows that the decay time will be a function of the conductor's resistivity and inductance. Better conductors will have low values of R and therefore will decay slower. The inductance is determined by the size of the deposit, thus the larger the deposit, the longer the decay time.

4 Airborne EM Geophysical Exploration Systems

4.1 Frequency Domain Systems

4.1.1 Quadrature Method

The first airborne system to be implemented to any scale used the *Quadrature Method.* In this system, the phase shift between the primary and secondary fields was measured. The contemporary version of this system was updated in the mid 1970s in order to use five frequencies. This system is no longer in use according to Telford *et al* [Telford90].

4.1.2 Airborne VLF

VLF (Very Low Frequency) signals are broadcasted by certain marine and navigation systems. This system was meant to be used for long range geolocation and is known as LOng RAnge Navigation LORAN. The concept was to build stations that would cover the entire globe such that three transmitter stations would be visible at all time by the receiver. The system is relatively well developed in North America but is not fully functional in the Eastern Hemisphere. The North American transmitters suitable for EM geophysical exploration are located in Cutler, ME, Annapolis, MD, Boulder, CO, Seattle, WA, and Hawaii. The Eastern Hemisphere is only covered by three large transmitters - Rugby, England, North Cape, Australia, and Moscow, Russia. More information on VLF communication can be obtained in work by Watt [Watt67].

The instruments using VLF were first introduced in the 1970s. A pair of whip antennas were mounted orthogonal to one another on an extension of the nose of the aircraft. They measured the E_x and the E_z fields while the flight path was normal to the transmitter direction. The phase quadrature between the two vectors was the quantity of interest. With this

quantity it was possible to determine the ground apparent resistivity, more details can be found in the work of Parasnis [Parasnis97] and Telford *et al* [Telford90].

4.1.3 Phase-Component Measurements

This technique is an adaptation of the moving source (horizontal-loop) method. In this method, both the transmitter and the receiver move down the traverse line. It is important that the distance between the transmitter and the receiver stay fixed. The primary field and the anomaly due to the aircraft are reduced as much as possible by a *bucking* coil and a balancing network. All of the other anomalies recorded are therefore due to conductors in the proximity of the system. Usually there are about five different frequencies in use in this system. The frequencies are selected as a function of the type of aircraft and the altitude at which the survey are done. The system can also be placed under a helicopter for lower altitude work. According to Telford *et al* [Telford90] higher frequencies are used for helicopter-borne equipment which decrease the depth of penetration, but increase the resolution of the system.

4.2 Time Domain Systems

4.2.1 INduced PUlse Transient System (INPUT)

The fundamental problem in airborne EM is the ability to measure a very small secondary field S while cancelling the continuous primary field P. When the system is stationary, the cancellation techniques work well, but once the system is set in motion, the vibrations induce strong noise signals. Most of the noise is created by the inappropriate cancellation of the primary field. The INduced Pulse Transient system *(INPUT)* developed by Barringer in 1962 pulses the primary field such that it is off for the measurement of the secondary field.

Telford *et al* [Telford90] say that it is considered to be the original airborne time domain system. Since the primary is switched off during the measurement time in this system, the only noise source from the vibration is caused by the motion in the Earth's magnetic field and the secondary field. This system has great claims to fame since it promises depth of penetration as great as 300 meters and the multichannel recording of the decaying field provides information on the nature of the conductor. This system was used as inspiration for the system being designed by Custom Research Ltd.

5 Magnetic Sensors

In Section 3.2 we saw that the secondary field is a magnetic field which decays slowly with time for good conductors. Slow varying fields in the TD translate to low frequency components in the FD. The sensors needed must be able to sense small magnetic fields which vary slowly with time. James Lenz [Lenz90] offers a good description of the most common magnetic sensors in use today. The magnetometers presented in this article can be divided in two categories; total field magnetometers and directional magnetometers.

5.1 Total Field Magnetometers

Sensors which fall into this category only give magnitude information about the magnetic field that is applied to it. The Optically pumped Magnetometer and the Nuclear-Precession Magnetometer fall into this category. The advantage of these magnetometers is that they can have great sensitivity without being prone to noise caused by vibration. For this reason, many of these magnetometers have been developed and are being used by exploration companies for airborne magnetic surveys. Unfortunately this resilience to vibration comes

at the cost of the loss of directional information.

5.2 Directional Magnetometers

These types of magnetometers only respond to flux which is directed along their sensitive axis. By using three orthogonal magnetometers, the orientation of the magnetic field can be resolved, providing important information to geoscientists. Unfortunately, this also means that signal processing must be used in order to remove vibration noise. This source of noise is very important since it generally dominates the noise sources in ATEM techniques. From all the available options, only two types of sensors seem to have spawned interest among the geophysical exploration community.

5.2.1 The Conventional Induction Magnetometer (CIM)

The design of the CIM is based on Faraday's law of induction presented in section 3. The following equation gives the general form of Faraday's law of induction

$$\nu = -N\frac{d\phi}{dt}, \tag{4}$$

where v is the voltage induced, N is the number of turns, and $d\Phi/dt$ is the time derivative of the flux. For a CIM under sinusoidal excitation, equation 4 takes the form seen in equation 5

$$V = \mu_o \mu_{core} N A \, j\omega H_o, \tag{5}$$

where V is the voltage induced, μ_o is the permeability of free space $4\pi \times 10^{-7}$, μ_{core} is the apparent permeability of the core, N is the number of turns, A is the cross sectional area of

the core, ω is the angular frequency of the field applied and H_o is the field strength of the magnetic field applied.

Early geophysical literature by Breen [Breen64] and Becker [Becker67] concentrates on air cored CIMs because their performance is easier to predict. Without the flux concentrating effect of a permeable core, these CIMs tend to be awkward to work with because of their size and weight. With the advent of new ferrite and alloys such as Mu-Metal® more development of cored CIM has been undertaken. This sort of CIM has been used in electromagnetic interference measurements [Hauser90], space exploration [Frandsen69, Lukoschus79], ELF/VLF communication [Watt67, Burrows78] and seismo-electric geophysics exploration[Kepic95]. Although some of the authors describe aspects of the theory associated with their coil design, the optimization parameters do not usually coincide with the objectives of ATEM.

5.2.2 Super Conducting Quantum Interference Device (SQUID)

Most recently, magnetometers based on Super conducting QUantum Interference Devices (SQUID) have been proposed as a replacement to the CIM for geophysical exploration[Foley99, Foley01, Panaitov01, Chwala01]. These devices are currently the most sensitive magnetic sensors in existence. The principles behind these relatively new magnetic sensors are covered in [Josephson62, Jaklevic64, Clarke89]. With the advent of high temperature superconductors, new high temperature SQUIDs are being developed. They are much less expensive to operate than their low temperature predecessors since only liquid nitrogen cooling *(77K)* is necessary instead of liquid helium *(4K)*. The latest results for geophysical exploration appear promising [Foley99, Foley01, Chwala01] but there remains much to do in order to optimize the system for airborne applications.

The greatest problem lies in the motion of the sensor in the earth's magnetic field and the noise associated with the surrounding electronics. Although the literature on this matter is scarce with regards to geophysical exploration, Magnetic Anomaly Detection (MAD) offers some answers. The purpose of MAD is to detect objects such as ships, explosives or submarines either from the sea [Clem95, Clem01] or from the air [Hirota00]. In the future, many of the advances made in the world of MAD will probably be ported to ATEM geophysical exploration.

6 Induction Magnetometers

6.1 Physical Description

Figure 2 illustrates the cross-section of a CIM where $2s_1$ is the length of the winding, $2l_c$ is the length of the core and $2r_c$ is the diameter of the core.

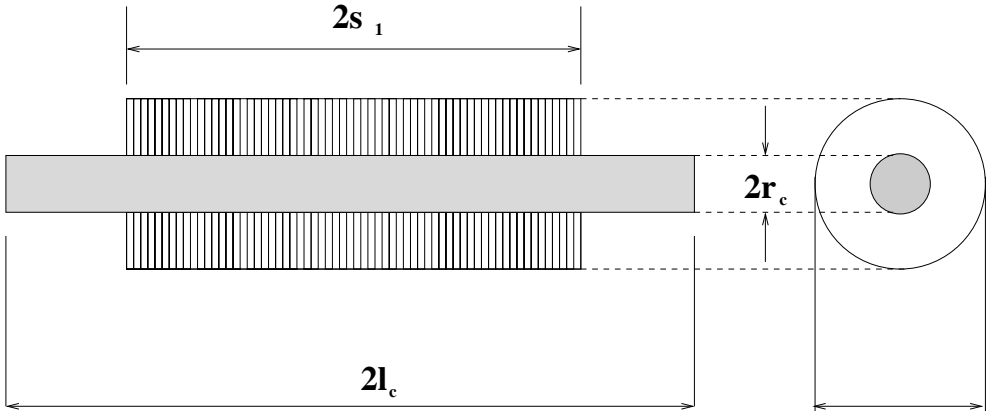

Figure 2: Cross-section of induction magnetometer

The total weight of the CIM, W_s, is due to the weight of the core W_c and the weight of the winding W_w as shown in equation 6

$$W_s = W_c + W_w \,. \tag{6}$$

The weight of the core can be computed by first computing the volume of the core V_c and then multiplying it by the density of the material used ρ_c

$$W_c = V_c \rho_c = \pi r_c^2 (2 l_c) \rho_c \,. \tag{7}$$

The weight of the winding can be computed in a similar fashion. The wire can be modeled as a long cylinder with radius r_w and length $2l_w$ as shown in equation 8

$$W_w = V_w \rho_w = \pi r_w^2 (2 l_w) \rho_w \,. \tag{8}$$

The density of the wire ρ_w , takes into account the density of the conductor and the insulator. Given the density ρ_w and the radius r_w, equation 9 can be used to determine the length of the wire which gives the prescribed winding weight W_w

$$2 l_w = \frac{W_w}{\pi r_w^2 \rho_w} \,. \tag{9}$$

Once the length of wire is known, the number of turns that can be wound around the core must be computed. The easiest case, is when the windings are orthogonal. Each turn is adjacent to the its neighbour, and the layers are completely filled before proceeding to the other.

In order to compute the number of turns possible in the winding region $2s_1$, the space is divided by the diameter of the wire d_w equation 10. This give the number of turns per layer N_{tl}

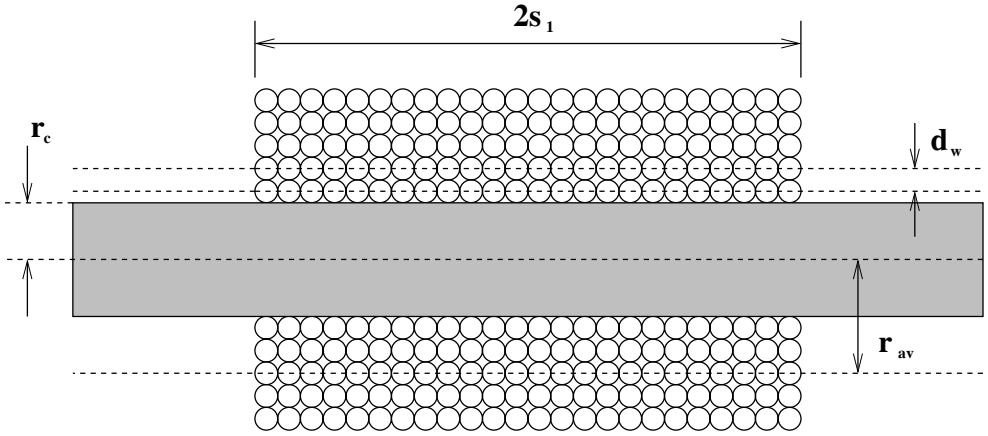

Figure 3: Orthogonal winding model

$$N_{tl} = \frac{2\,s_1}{d_w}\,. \tag{10}$$

In order to obtain the total number of turns, the number of turns per layer N_{tl} is multiplied by the number of layers N_{layers}

$$N_t = N_{layers}\,N_{tl}\,. \tag{11}$$

The length of the wire required $2l_w$ to make N_t turns can be computed by taking the average turn circumference and multiplying by N_t

$$l_w = N_t\,\pi\,r_{av}\,. \tag{12}$$

Combining equation 9 and equation 12, allows one to compute the total number of turns given the weight of the winding

$$N_t = \frac{W_w}{2\,\pi^2\,r_w^2\,r_{av}\,\rho_w}\,. \tag{13}$$

Unfortunately, the orthogonal winding technique is not usually used for induction magnetometer. The closely spaced windings create capacitance which causes the CIM to self resonate. This resonance limits the usable bandwidth and therefore is usually avoided, see Section 6.2 for more details. In order to limit the winding capacitance *scramble* winding is usually used. This winding technique distributes the turns in a pseudo-random fashion. Layers are not completely filled before proceeding to the next one. Although the spacing introduced decreases the capacitance, it increases the length of wire required to make the same number of turns and thus increases the weight and the resistance of the winding.

Lukoschus [Lukoschus79] proposed to modify the equations for orthogonal windings in order to include the filling factor. In the experience of this author, the equations proposed led to confusion and inaccurate results. For this reason, a more general approach was taken which describes the wire as layers of multiple helixes.

The helix was described by parametric equation 14 found in work by Stewart [Stewart95]. Figure 4 illustrates the basic shape of the helix to be used as a building block in this work

$$r(t) = A_r \cos(t)\,\vec{i} + B_r \sin(t)\,\vec{j} + C_r t\,\vec{k}, \tag{14}$$

where A_r, B_r and C_r provide the scaling factors in the i , j and k directions. The variable t is used to increment the position along the helix.

In our case, the helix is wound around cores which are cylindrical, thus $A_r = B_r = r$ and $C_r = 2s_1$. The length of the helix can be computed by evaluating the following integral

$$l_l = \int_0^{2\pi N} \sqrt{\left(\frac{dx}{dt}\right)^2 + \left(\frac{dy}{dt}\right)^2 + \left(\frac{dz}{dt}\right)^2}\, dt \tag{15}$$

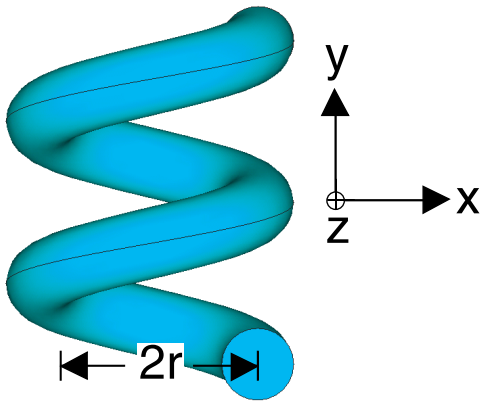

Figure 4: First two turns of a winding

$$\frac{dx}{dt} = -r\sin(t)$$
$$\frac{dy}{dt} = r\cos(t)$$
$$\frac{dz}{dt} = 2s_1\,,$$

where N is the number of times a full revolution will be done around the core for the set layer. Solving equation 15 yields equation 16

$$l_l = 2\sqrt{r^2\pi^2N^2 + 4s_1^2\pi^2N^2}\,. \tag{16}$$

The helix describes the trajectory of the middle of the wire around the core. This means that according to figure 3

$$r = r_c + \frac{d_w}{2}. \tag{17}$$

In order to compute the total number of turns possible with a specified length of wire, a computer program was created. The first step was to determine the number of turns which could be accomplished given the specified spacing between the turns. Like in the case of the orthogonal winding, the number of turns per layer N_{tl} was determined using equation 10. In the case of the *scramble* winding, not all of the layer would be filled before proceeding to the next layer. The amount of the layer which was filled was represented by the fill factor γ_f. This meant that for a scramble wound winding , the number of turns per layer was defined by equation 18

$$N_s = N_{tl}\gamma_f \quad [0 < \gamma_f < 1\ ]. \tag{18}$$

When multi-layered windings were wound, the winding radius would increase at every layer such that equation 17 could be modified to

$$r = r_{core} + n_{layer}\left(\frac{d_w}{2}\right). \tag{19}$$

The layers were progressively filled by the computer program until a complete layer was not possible. The remaining turns were computed by re-arranging equation 16. The turns remaining on the last layer N_{ll} were computed with equation 20

$$N_{ll} = \frac{\sqrt{l_{wl}^2 - 4s_1^2}}{2r\pi}. \tag{20}$$

The extra turns of the last layer were added to the number of turns of the filled layers.

This gave the total number of turns that could be wound around a core given the specified filling factor.

6.2 Electrical Description

The simplest way of looking at a CIM was to treat it as a voltage source in series with a *real* inductor. This was the approach that was taken by Kepic [Kepic95] and Hauser [Hauser90]. The model found in figure 5 was the model which they proposed.

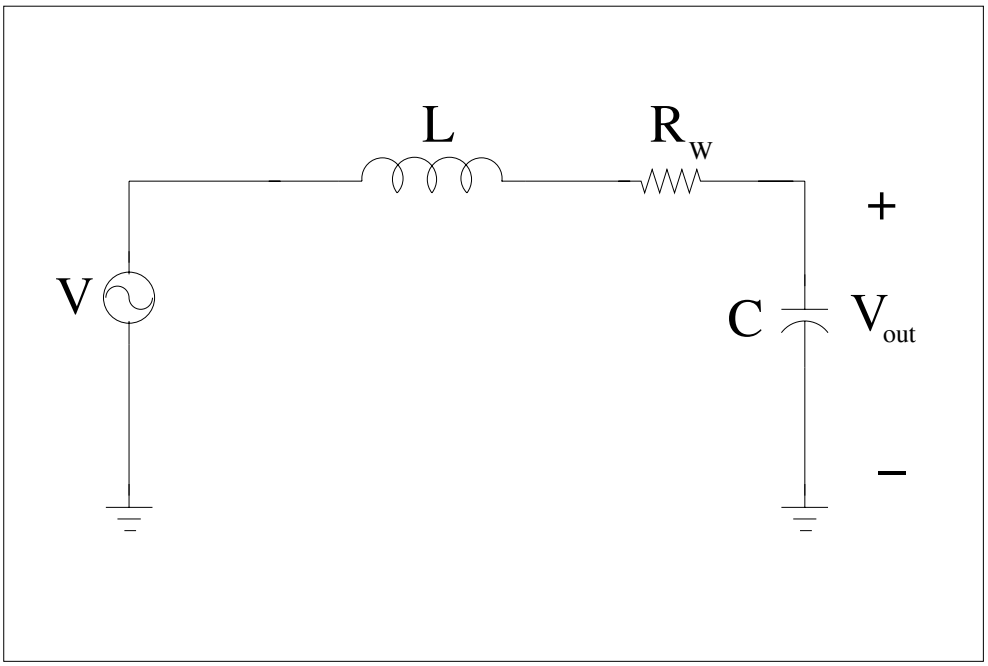

Figure 5: Basic model of an inductor

This model is only partly accurate, since it assumes that the core is lossless. When ferrites with high resistivity are used this assumption is valid, however materials such as Mu-Metal ® have resistivity that are small enough to cause the model to change. A more accurate model is proposed by C&D Technologies [CDtechnologies]. The SPICE model

used for real inductors is found in figure 6.

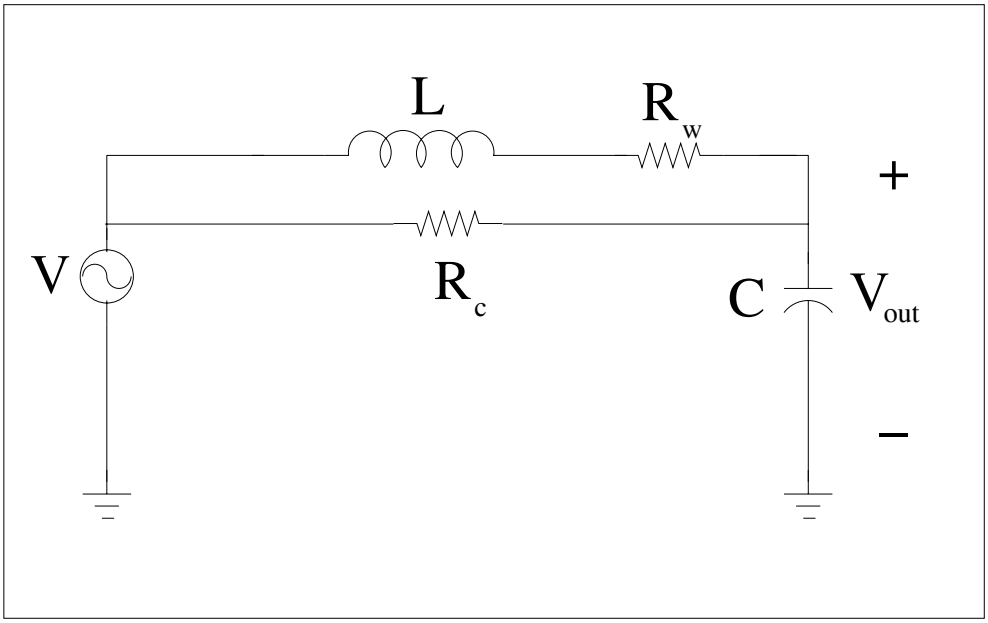

Figure 6: Model of an inductor adapted from C&D Technologies [CDtechnologies]

When the resistivity of the core material is small, eddy currents are induced in the core material. These currents flow around the core in such a way as to produce fields which oppose the flux. Because of this flux opposition, all the flux does not pass through the core and thus the core does not have the flux concentrating effect sought. In order to avoid eddy current problems in materials such as Mu-Metal® the laminations must be sufficiently small and directed along the length of the core. Slemon [Slemon66] proposes equation 21 to model the losses due to eddy currents

$$R_c = \frac{N^2 A_c}{\widetilde{l}} \frac{12\rho}{c^2}, \tag{21}$$

where R_c represents the losses due to eddy currents, A_c is the cross-sectional area of the core, $\widetilde{l}$ is the mean length of flux path, c is the lamination thickness, N is the number of turns

and ρ is the resistivity of the core material. According to Slemon [Slemon66], the usual thickness of lamination for the audio frequency range is between 0.02 mm and 0.05 mm. The CIMs of interest operate in the same frequency range as baseband audio and thus these lamination thicknesses should be used as a guide for lamination of a core.

The other resistance term R_w arises from the incremental resistivity of the wire used in the construction of the winding. It can be calculated by using equation 22 from [Boylestad94]

$$R_w = \rho_{wire} \frac{l}{A_w}, \tag{22}$$

where ρ_{wire} is the resistivity of the conductor, l is the length of the conductor and A_w is the cross sectional area of the wire. The resistance has an impact on the level of thermal noise and the Q of the search coil. According to Lukoschus [Lukoschus79], the winding thermal noise voltage dominates Nyquist and Barkhausen noise coming from the core by several orders of magnitude and thus is the only one of interest. The thermal noise voltage is caused by the random motion of electrons in the resistor. The general form for the noise voltage is defined by equation 23 found in work by Pozar [Pozar98]

$$v_n = \sqrt{4kTBR}, \tag{23}$$

where k is Boltzmann's constant, T is the temperature in Kelvin, B is the bandwidth in Hz and R is the resistance of the winding.

The Q of the coil is given by the relationship of inductive reactance to the resistance of the coil as described by equation 24 from Boylestad's work [Boylestad94]

$$Q = \frac{X_L}{R} = \frac{2\pi f_o L}{R}. \tag{24}$$

The value of the inductive reactance is computed at the self resonant frequency of the search coil. This self-resonance is caused by the presence of distributed capacitance among the winding. Each turn which composes the winding has an amount of capacitance with its neighbours. The final capacitance value depends on the winding techniques, the size of the insulation and the type of insulation. Equation 25 gives this resonance

$$\omega = 2\pi f_o = \sqrt{\frac{1}{LC}} \rightarrowtail f_o = \frac{1}{2\pi}\sqrt{\frac{1}{LC}}\,. \tag{25}$$

The easiest way to obtain the capacitance is by measuring the self-resonant frequency f_o of the CIM and to calculate C by re-arranging equation 25 such that

$$C = \omega^2 \frac{1}{2\pi f_o L}\,. \tag{26}$$

From experiments described in section 12.1, it was discovered that the capacitance of the CIM becomes stable once a large number of turns have been spooled onto the core. Given the relative stability of C for a large number of turns, the parameter which has the most influence on the frequency of self-resonance is the inductance L.

Boylestad's introductory text [Boylestad94] approximates the self-inductance of a search coil by the self-inductance of a long solenoid. This is given by equation 27.

$$L = \mu_o \mu_c \frac{N^2 A}{l_c}\,. \tag{27}$$

This equation works well for air-cored search coils or coils for which the length of the core is infinite with respect to its diameter since the flux can be assumed to be uniform. Consequently, it fails to account for the variation of the flux within a *finite* permeable rod core. The variation of the flux within the core is caused by flux lines which do not enter

and exit from the ends of the core as is shown in figure 7.

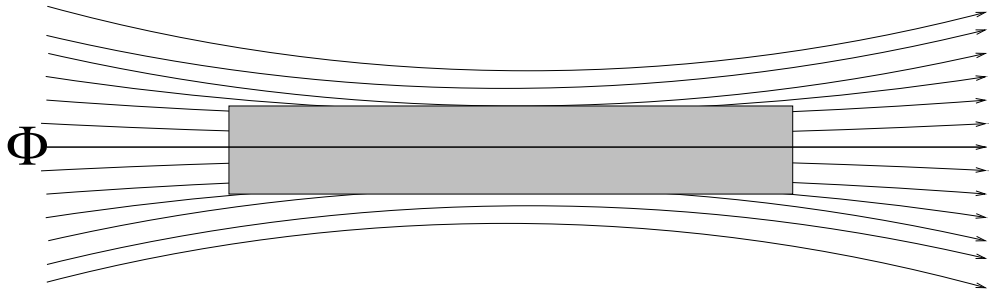

Figure 7: Flux lines in permeable core

Since the inductance is related to the amount of flux which threads the coil, this flux variation has a significant impact on the observed inductance and on the induced voltage. This variation of flux along a permeable core at ELF was found to be similar to the current profile of a short electric dipole antenna as described in the work of Kaplan *et al.* [Kaplan98, Kaplan94, Kaplan02]. The original work done by Kaplan *et al.* [Kaplan94, Kaplan98] illustrated that this was the case for small coils centered at the middle of the rod. Equation 28 for the inductance of a small coil centered about the middle of a permeable core was obtained from this work

$$L = N^2 \frac{\pi \mu_o l_c}{\ln(\frac{2l_c}{r_c} - 1)}. \tag{28}$$

Kaplan *et al.* [Kaplan02] demonstrates that this theory holds true for windings which occupy a much larger portion of the core. The inductance found with equation 28 is corrected for the flux variations by multiplying it by the integrated flux weighting function. The weighting function has a triangular shape similar to the current profile of a small dipole and is described by equation 29 from Kaplan's work [Kaplan02]

$$I_m(s) = \begin{cases} 1 + \frac{s}{l}, & -l \leqslant s \leqslant 0 \\ 1 - \frac{s}{l}, & 0 \leqslant s \leqslant l \end{cases} . \tag{29}$$

The flux weighting function is illustrated in figure 8.

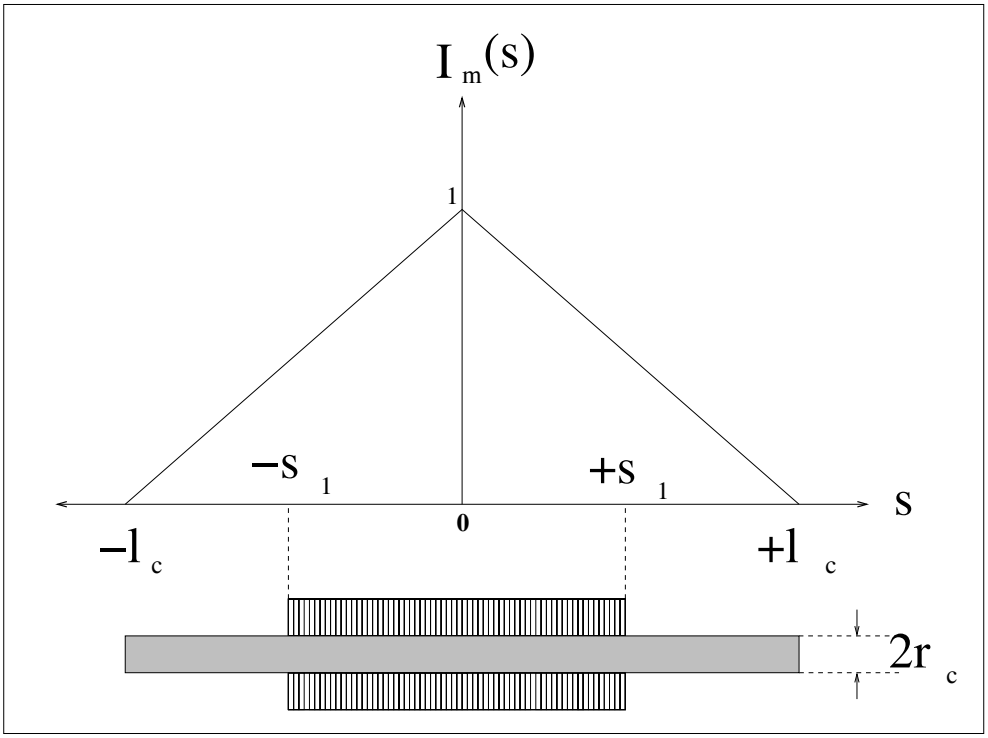

Figure 8: The flux weighting function $I_m(s)$ adapted from [Kaplan02]

After multiplying by the integral of the flux weighting function, equation 28 is transformed into equation 30

$$L = \left(N^2 \frac{\pi \mu_o l_c}{\ln(\frac{2l_c}{r_c} - 1)} \right) \left(1 - \frac{s_1}{2l_c} \right) . \tag{30}$$

The only complicating element left out during this discussion is the demagnetization factor. The apparent permeability of a cylindrical core is generally much different than

the initial permeability of the material of which it is made [Bozorth42, Bozorth93]. In this discussion, it is assumed that the initial permeability is high enough and the length-to-diameter ratio is small enough for the permeability to be geometry limited. In order to ensure that this assumption is valid, the apparent permeability of the core should be found by using figure 9 taken from Bozorth's work [Bozorth93].

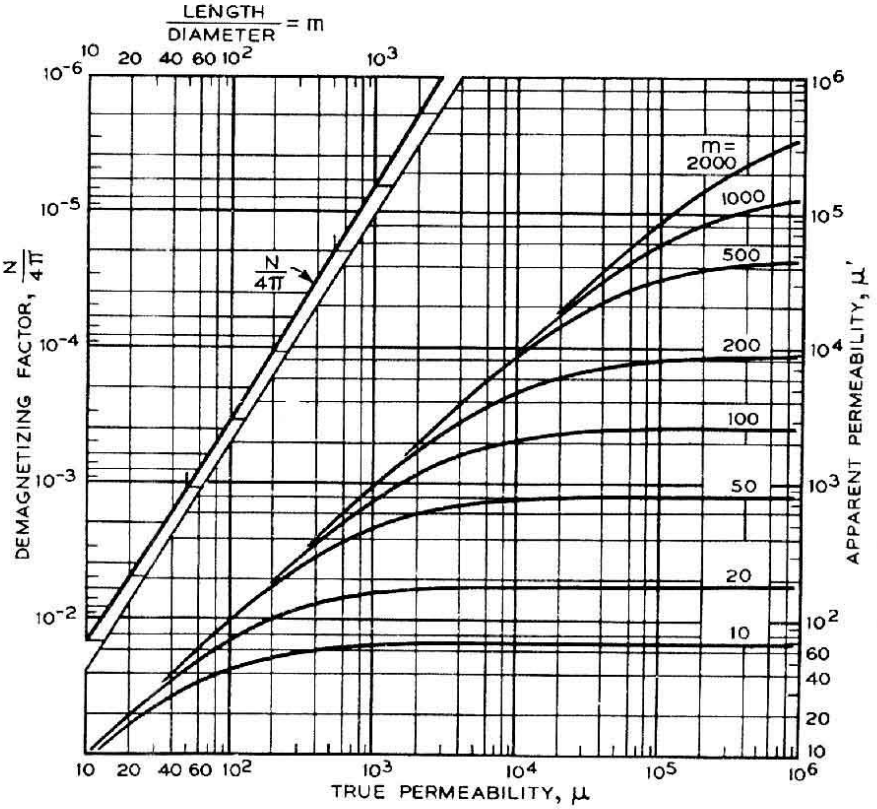

Figure 9: Effects of the length-to-diameter on apparent permeability [Bozorth93]

The x-axis labeled as the "TRUE Permeability, μ" is in fact the initial permeability of the material used in the core. The y-axis on the right reveals the apparent permeability that will be observed for the various cylindrical cores. The family of curves traced reveal the

attainable apparent permeability given a set initial permeability and the length-to-diameter ratio of the core. The apparent permeability of the core of CIM can either be geometry limited or permeability limited. When the core of a CIM is geometry limited, changing the core material for a core with a higher initial permeability does not give higher apparent permeability. For example, suppose that we have a core which is made of a material with an initial permeability of 1000 and has a length-to-diameter ratio of 10. The apparent permeability of the core will be approximately 60. Suppose that we replace the core with a geometrically identical core made of a material with an initial permeability of 10000. The apparent permeability will still be approximately 60. The core of the induction magnetometer can also be permeability limited. For example, suppose that we have a core with an initial permeability of 1000 and a length-to-diameter ratio of 200, the apparent permeability will be approximately 1000. If the same material is used to make a core that has a length-to-diameter ratio of 500, the apparent permeability will remain at approximately 1000.

It was noted earlier that the flux distribution had an effect on the inductance of the CIM, but it also has an influence on the induced voltage. In equation 5, it was assumed that the flux was uniform inside the area enclosed by the windings. This is obviously not the case for CIMs which have a finite length core.

In order to compute the induced voltage with accuracy, it is important to look at the problem from the fundamentals. From [Kaplan94] the flux for a long ellipsoid is defined by equation 31

$$\phi = \frac{\pi \mu_o l_c^2 H_o}{\ln\left(\frac{2l_c}{r_c}\right) - 1}, \tag{31}$$

where H_o is the magnetic field strength that is to be measured.

The contribution of the different sections of the core to the total flux can be taken into account by integrating along the flux weighting function as is done in [Kaplan02]. This yields equation 32

$$\phi_c = \left(\frac{\pi \mu_o l_c^2 H_o}{\ln\left(\frac{2l_c}{r_c}\right) - 1} \right) \left(\frac{1}{s_1} \int_0^{s_1} (1 - \frac{s}{l_c}) ds \right) \tag{32}$$

Integrating 32, we get equation 33

$$\phi_c = \left(\frac{\pi \mu_o l_c^2 H_o}{\ln\left(\frac{2l_c}{r_c}\right) - 1} \right) \left(1 - \frac{s_1}{2l_c} \right) . \tag{33}$$

In section 5.2.1 Faraday's law of induction, equation 4, was presented. From this law, the induced voltage in a cylindrical core is

$$V = -N \left(\frac{\pi \mu_o l_c^2 H_o}{\ln\left(\frac{2l_c}{r_c}\right) - 1} \right) \left(1 - \frac{s_1}{2l_c} \right) j\omega . \tag{34}$$

7 Noise Sources

As in any system, geophysical exploration systems are subject to noise. The secondary field from the conductive target is very weak and can easily be lost amongst all of the noise. Some noise sources are inherent to the measurement environment while others are introduced by the measuring system. The two different types are discussed in this section and their relationship is explained. ATEM surveys have different characteristics than other applications and the concept of noise is also different. The raw data collected during a survey is generally subjected to a lot of post-processing in order to obtain the signal of interest and to cancel the interfering signals. This differs from communication systems

where the ambient noise will generally limit the usefulness of a communication channel. The objective is to design sensors with large dynamic range which can accommodate the signal of interest in addition to the noise. The noise from the sensing system constitutes the noise floor of the survey system. No post processing can be employed to remove this noise source. McCracken *et al.* [McCracken86] offers a good introduction to the common noise sources encountered in electromagnetic exploration systems. The noise sources which are identified in the work by McCracken *et al.* [McCracken86] are related to the environment where the survey is done and the methods used. The upper limit of the dynamic range is specified by these noise sources and the primary field of the transmitter. The following reviews the environmental noise and the instrumentation noise present in a geophysical survey system.

7.1 Electromagnetic Noise

7.1.1 Cultural Noise

This noise is caused by civilization and is generally assumed to be phase-coherent. Power grids and low frequency wireless communications are usually the sources. According to McCracken *et al.* [McCracken86], all of the modern exploration systems have circuits which can easily reject phase-coherent cultural signals thus making it of little concern. According to Randa [Randa95], the typical magnetic field strength for representative human environments due to power lines is 0.16 μT. Extensive work has also been done by Butler and Russell [Butler03] in order to cancel multiple harmonic noise series from geophysical records at the post-processing stage.

7.1.2 Natural Noise

Variations in the geomagnetic field, sferics and solar flares account for the rest of the noise observed while the receiver is stationary. Sferics are electromagnetic radiation caused by severe weather condition such as lightning discharge. Burrows [Burrows78] describe the concept of the ionosphere waveguide, its propagation characteristics and noise caused by sferics which he lists as the most important noise source in ELF (30 Hz - 3 kHz). He also points out that the earth-ionosphere cavity can resonate. This principle was first discovered by Schumann after which this resonance is named. The first three Schumann resonances occur at 7, 14 and 21 Hz. The power spectrum of this signal varies greatly depending on the time of day and the weather conditions which affects the shape of the ionosphere. Some higher order harmonics have been recorded before, but they are usually insignificant. This resonance is not expected to be a large obstacle since it is only observable when the atmospheric noise at the test site is low. In general lightning activity will dominate the atmospheric noise. Extensive work was done by Maxwell [Maxwell67] in order to quantify the atmospheric noise around the world. He also came to the conclusion that the atmospheric noise was dominated by sferics and that their effect was worst around the equator where thunderstorm activity was usually greatest. According to McCracken *et al.* [McCracken86], the noise caused by lightning strikes is essentially random in time and thus can be partially removed by averaging over time or by increasing the level at the transmitter. Robust statistical methods of reducing sferics noise are also presented in Buselli *et al.*[Buselli96].

7.2 Geologic Noise

In section 2 it was stated that exploration techniques are generally based on the physical characteristics of the deposit and its surroundings. If a deposit was not different than its surroundings, it would be very difficult to find. On the other hand, if the deposit was suspended in a well defined, non-conductive, homogeneous ground, only the target would react to the excitation and thus would be easily detected. The ground is made up of a variety of rocks and minerals which share common boundaries and are covered-up by a layer of soil. This layer is called the overburden and its characteristics vary extensively around the world. Its thickness is irregular and can vary from a zero meters to several hundreds of meters. In arid zones the conductance of the overburden can be as high as 50 siemens while it can be less than 0.1 siemens in recently glaciated terrains [McCracken86]. These variations in the overburden mean that it also generates a response to the exciting field which causes many problems. Entire ore deposits can be missed in arid regions when the response of the overburden masks the response from the deposit below. This problem does not affect TEM systems as much as *Frequency ElectroMagnetic* (FEM) systems because the response of the overburden is strongest during the initial phase of the excitation. Later time samples provide the information about the buried conductor and are free of overburden artifact. McCracken *et al.* [McCracken86] points out that there exists an optimum to the time delay. The survey condition should be well understood before making measurements and interpreting the data. The survey design is best left to geophysicists who understand the relationships between the different rock formations and their weathering pattern. With this knowledge they can assess the expected level of geological noise and determine the appropriate time delays at the transmitter.

7.3 Operation Noise

In the case of FEM systems a large part of the noise comes from misalignment and improper cancellations of the primary field. The secondary field is present among the primary field and the response of the overburden. McCracken *et al.* [McCracken86] explains methods which can help reduce the operational noise for FEM systems. In the case of a TEM system, the transmitter is turned off during the measurement stage, therefore the operational noise is much lower. The operational noise which remains is caused by its movement in the earth's magnetic field. According to Munkholm [Munkholm97], the advent of three axis magnetometers makes it possible to reduce the motion induced noise from vibration of a moving TEM receiver.

7.4 Instrumentation Noise

CIMs are self-resonant devices as was pointed out in section 6.2. Given the large inductance values, this resonance often occurs within the frequency band of interest. The large Q of the circuit causes the CIM to ring for a long period of time when it is excited by a step function. This instability overwhelms the response of the CIM and it cannot be used as a broadband magnetic sensor. Two different types of compensation circuits were investigated in this work. The first was to introduce a damping resistor in parallel with the CIM. The second method was to use a current to voltage converter as proposed by Hauser [Hauser90] and Macintyre [Macintyre80].

7.4.1 Damping Resistor

This compensation technique is the most popular given its simplicity. Figure 10 illustrates the equivalent circuit of the CIM with the introduction of the damping resistor.

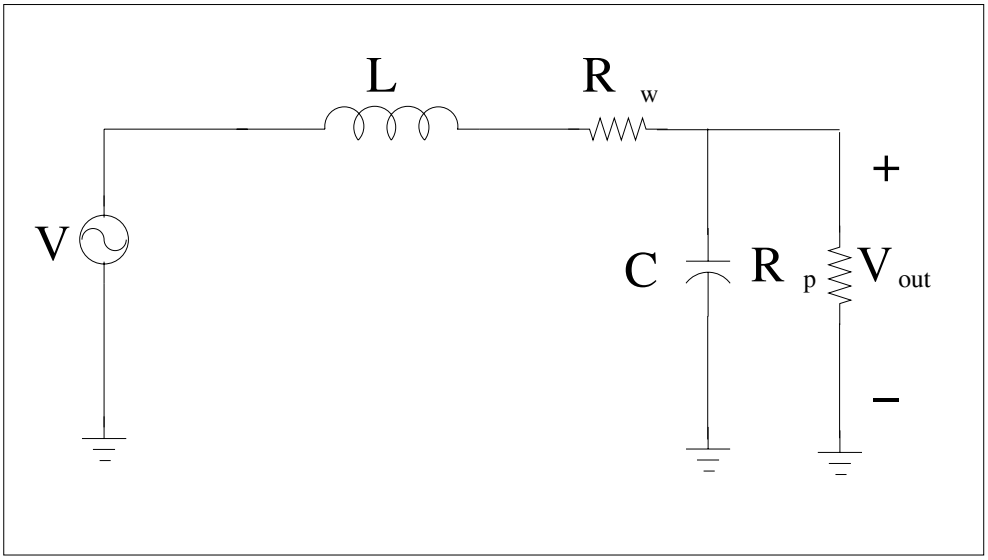

Figure 10: Classical R_p compensation.

Although the winding capacitance C is partly responsible for the self-resonant behavior of the CIM, Hauser [Hauser90] and Macintyre [Macintyre80] argue that it can be left out of the discussion for the noise of the circuit. The circuit contained in figure 10 can be redrawn with the noise sources of the circuit as shown in figure 11.

The new variables introduced E_w^2 and E_{tp}^2 are respectively the thermal noise attributed to the winding resistance R_w and the damping resistance R_p. Using an example from Motchenbacher *et al.* [Motchenbacher93], the noise reffered to the input of the preamplifier in figure 11 can be written as

$$E_{no}^2 = E_w^2 \left(\frac{R_p}{Z_1 + R_p} \right)^2 + E_n^2 + \left(I_n^2 + I_{np}^2 \right) \left(\frac{R_p Z_1}{Z_1 + R_p} \right)^2, \tag{35}$$

where $Z_1 = R_w + j\omega L$, E_n is the noise voltage and I_n is the noise current of the preamplifier to which it will be attached, and $I_{np} = \sqrt{4kT/R_p}$ where k is Boltzman's constant and T is the temperature in Kelvins. The noise referred to the input of the CIM can be calculated by

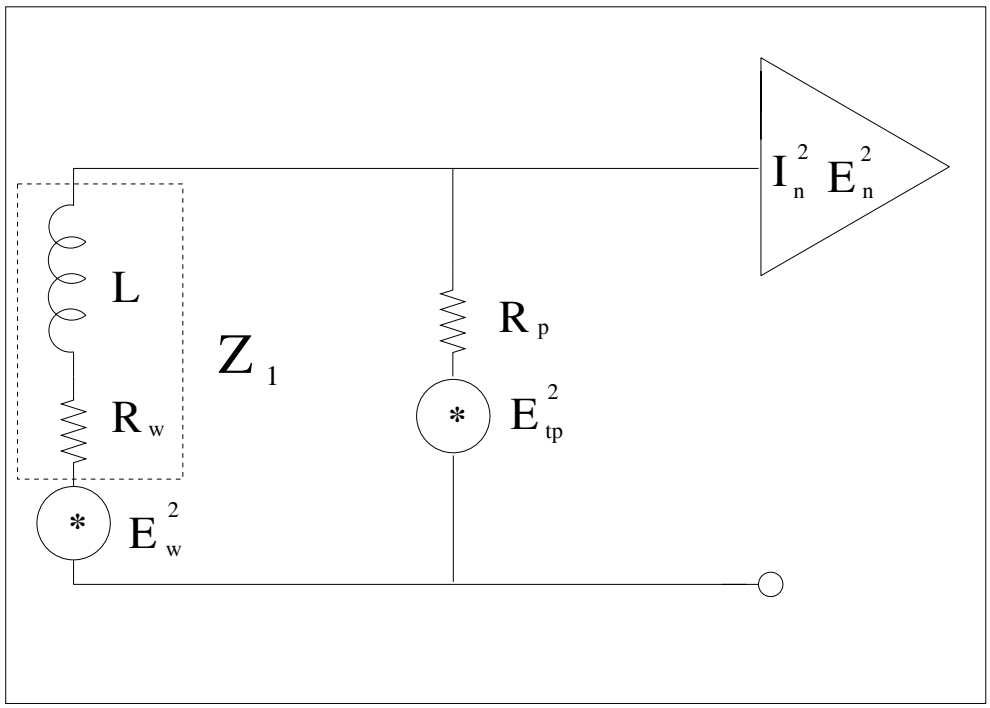

Figure 11: Classical R_p compensation noise model.

dividing equation 35 by the gain of the circuit such that

$$E_{ni}^2 = E_w^2 + E_n^2 \left(\frac{Z_1 + R_p}{R_p}\right)^2 + \left(I_n^2 + I_{np}^2\right) Z_1^2 . \tag{36}$$

From equation 36 we see that in order to keep noise low, R_p should be as large as possible, while Z_1 should be made as small as possible. Both values are dependent on the behavior of the CIM. Recall that the induced voltage is proportional to the number of turns N, and that its inductance is related to N^2. The higher the Q of the CIM, which is related to the inductance and winding resistance, the lower the value of R_p needed to damp the resonance and thus the larger its noise contribution.

7.4.2 I-to-V Converter

The second option to eliminate self-resonance is to treat the CIM as a current source and use an I-to-V converter to transform the current into a voltage. The circuit proposed by Hauser [Hauser90] and Macintyre [Macintyre80] is found in figure 12.

In order to do the noise analysis, figure 12 was redrawn with the appropriate noise sources included in the diagram.

Hauser [Hauser90] and Macintyre [Macintyre80] argue that the capacitance C and C_f are not significant in the noise model and that C_f is only introduced for stability. This will also be assumed for this case. The output noise, E_{no}^2 can be written by superposition as

$$E_{no}^2 = E_w^2 \left(\frac{R_f}{Z_1}\right)^2 + E_n^2 \left(\frac{R_f}{Z_1}\right)^2 + I_n^2 R_f^2 + E_{nf}^2 , \tag{37}$$

where $Z_1 = R_w + j\omega L$ and E_{nf} is the thermal noise associated with the feedback resistor. Similarly, the input referred noise can be obtained by dividing the noise by the power gain

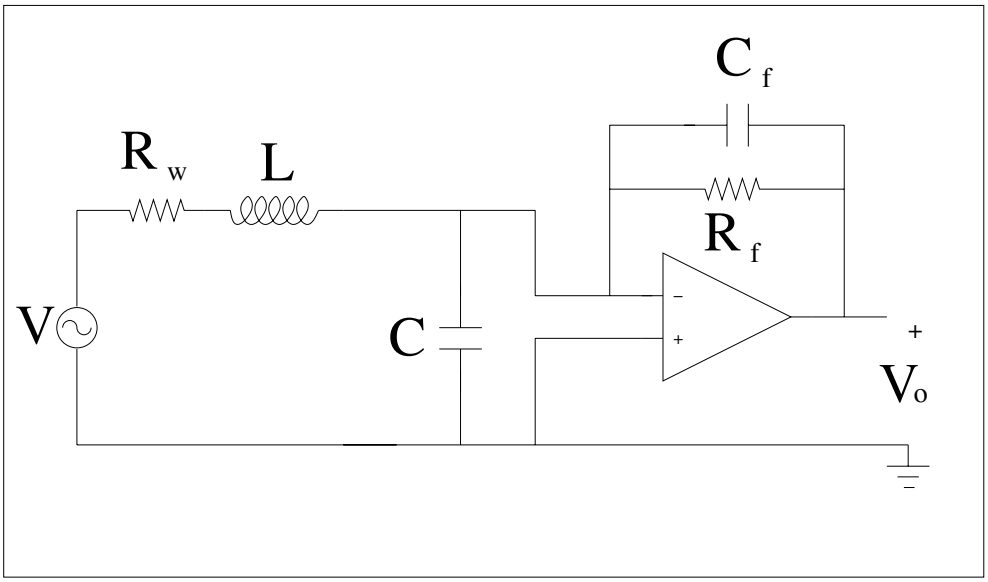

Figure 12: I-to-V converter as a compensation circuit

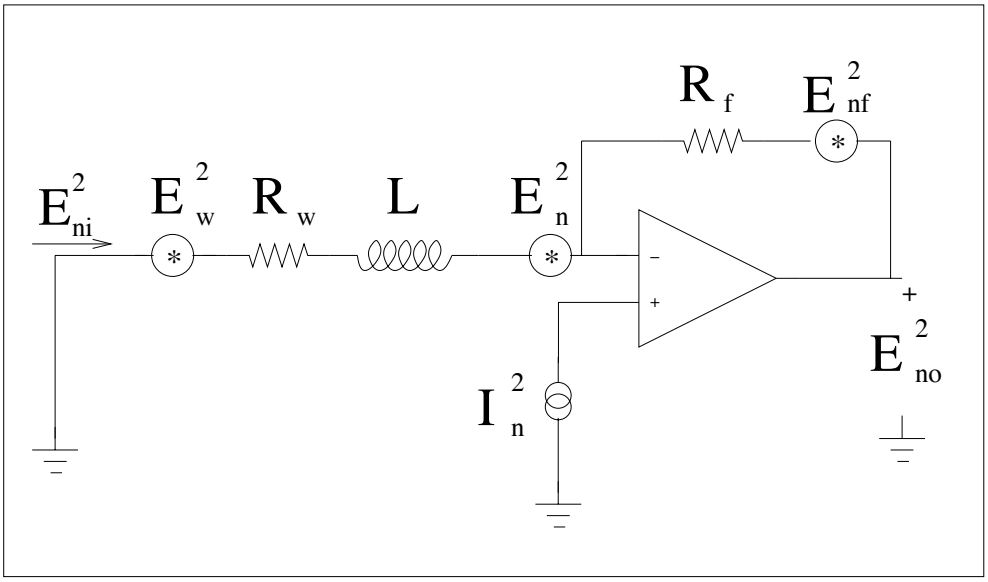

Figure 13: Equivalent noise circuit for I-to-V converter

which yields

$$\begin{gathered} E_{ni}^2 = E_w^2 + E_n^2 + I_n^2 (Z_1)^2 + \left(\frac{E_{nf}}{R_f}\right)^2 (Z_1)^2 \\ \textit{but } I_{nrf}^2 = \frac{E_{nf}^2}{R_f^2} \\ \therefore E_{ni}^2 = E_w^2 + E_n^2 + \left(I_n^2 + I_{nrf}^2\right) (Z_1)^2 . \end{gathered} \tag{38}$$

Equation 38 gives similar results to equation 36. Once again R_f must be as large as possible and the input impedance should be kept to a minimum. The advantage of the I-to-V converter is that the negative feedback allows stable operation even for very large values of R_f such that its impact on the overall noise is minimal. The limiting factor for noise is once again the impedance of the CIM.

8 Design Space

Given unlimited space, weight and financial means, we could build very large CIMs such as the ones used for micro-pulsation research at the Dallas Geomagnetic center [Green67]. These coils allow measurements of effects of magneto-hydrodynamic waves on low frequency (10^{-4}-10^{0} Hz) fluctuations in the Earth's magnetic field. Unfortunately, space, weight and budget all have limits imposed by physical realities, such as gravity. The six foot long Mu-Metal® cores used are much longer and heavier than could ever be accommodated by the helicopters available. Economics play a major role since the price of the helicopter rental constitutes a large part of the survey cost. The heavier the load, the larger the helicopter and the greater the expense.

First, consider equation 5. The induced voltage V depends on the number of turns N, the area of the core A, and the apparent permeability of the core μ_{core}. The frequency depen-

dence $j\omega$, the permeability of free-space μ_o, and the field strength H_o can be ignored since they exist independently of any physical variables that can be optimized. The area A and the apparent permeability μ_{core} are directly related to the shape of the core, while the number of turns N is only related by proxy. The shape of the core will influence the length of wire needed to complete the number of turns, and thus the resistance of the magnetometer, but in order to keep things simple, the first part of the optimization is done only on the variables directly related to the core. The optimization is thus going to be concerned with the result of the *Area-Permeability* product. An increase in either the area or the permeability yields an increase in the sensitivity of the induction magnetometer.

The length of the core $2l$ and its diameter $2a$ have an effect on the apparent permeability of the core and its area. As the length of the core increases, it approaches the condition where the length to diameter ratio is infinite. At this ratio, the apparent permeability equals the initial permeability. Figure 9 presented by Bozorth [Bozorth42, Bozorth93] demonstrate the effects of the length to diameter ratio on the apparent permeability. Figure 14 presents some of the data found in Bozorth's work [Bozorth93].

It is important to note that materials are limited by their initial permeability, thus even if a ferrite with initial permeability of 6500 was to have a length to diameter ratio of 1000 its permeability would never reach 300000, but would be limited to 6500.

For ATEM there are usually limits imposed on the overall length of the CIM. If we assume that the CIM is designed to meet these limits, the only way to increase the length-to-diameter ratio is to make the diameter smaller. Figure 15 illustrates the impact this has on the apparent permeability, and the area of the core.

From figure 15, we see that by decreasing the diameter of the core we gain permeability but we loose area. The impact on the area permeability product can be seen in figure 15.

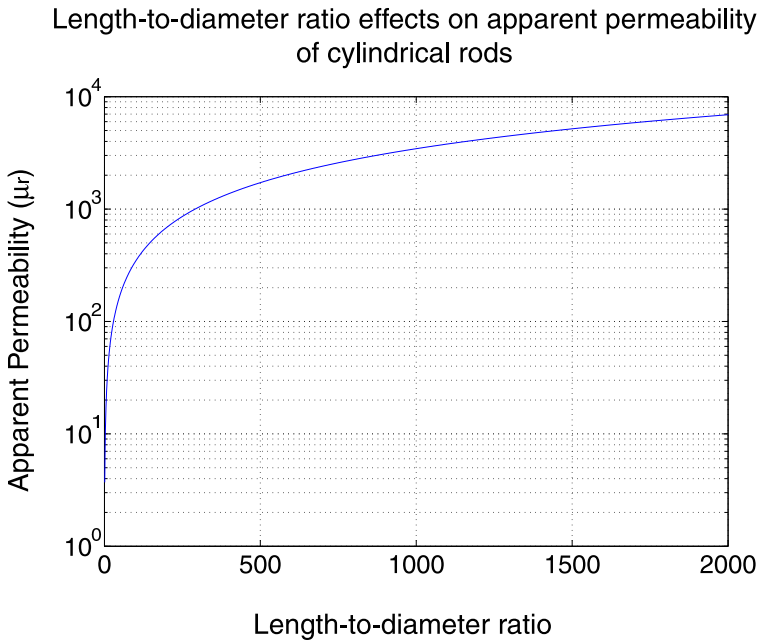

Figure 14: The impact of the length-to-diameter ratio on the apparent permeability

Figure 15 would let us suppose that we gain by increasing the area of the core rather than its length. From Faraday's law of induction equation 4, this also appears to make sense since a larger area will enclose more flux. The disadvantage with this approach is that by increasing the area, the weight of the core and its size rapidly becomes a problem. The reader should remember that the use of the core is to concentrate the flux and make the sensor lighter and more portable than the air cored CIM.

The next step of the analysis is to enter weight information on figure 15. The length to diameter ratio is defined as

$$\begin{aligned} n &= \frac{2l_c}{2r_c} = \frac{l_c}{r_c} \\ \therefore r_c &= \frac{l_c}{n}\,. \end{aligned} \tag{39}$$

The equation for the weight of the core was introduced in section 6.1 as equation 7.

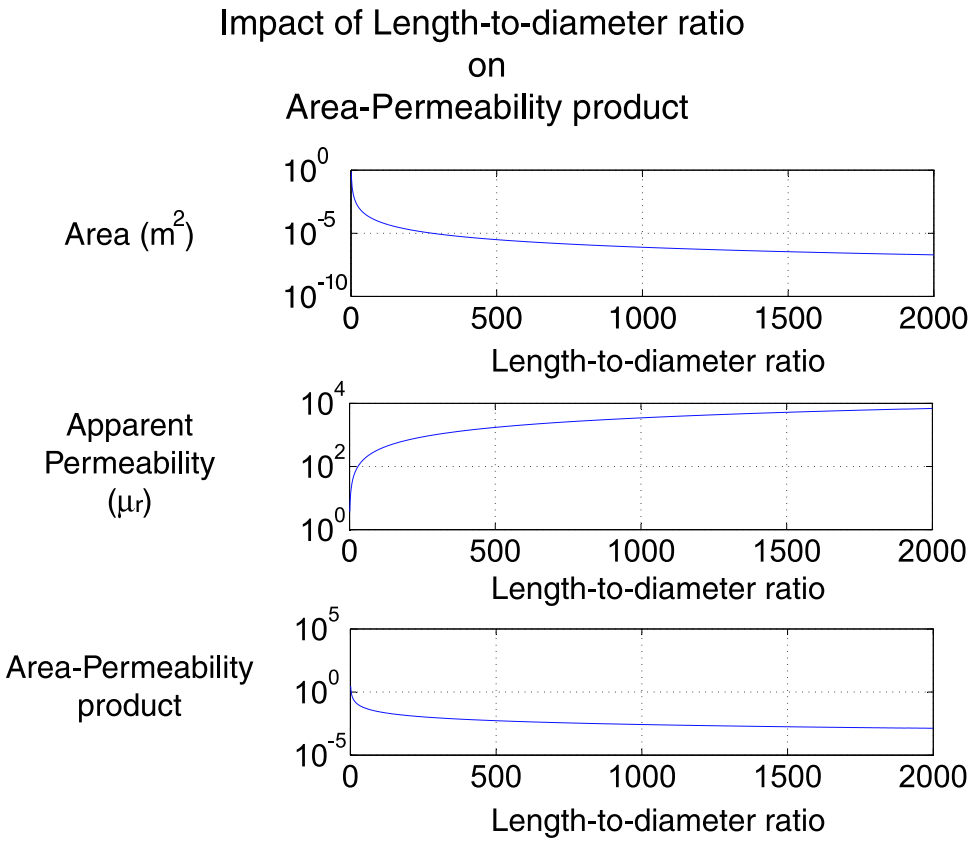

Figure 15: Effects of reducing the diameter of the core of a CIM

Substituting for r_c in equation 7 , we get equation

$$W_c = \frac{2\pi l_c^3 \rho_c}{n^2}. \tag{40}$$

Equation 40 can be re-arranged to solve for n which yields equation

$$n = \sqrt{\frac{2\pi l_c^3 \rho_c}{W_c}}. \tag{41}$$

Equation 41 allows us to determine the Area-permeability Product of a core of known weight and length. Figure 16 illustrates the results for a core made of MN60 and 60.96 cm in length.

As is seen in figure 16, the weight of the core increases rapidly, compared to the effects of the increase of area on the Area-Permeability product. The same basic approach can be taken to develop a model which stems from the amount of flux that threads the core. Using the definition of the length-to-diameter, equation 39, equation 31 can be re-written as

$$\Phi = \frac{\pi \mu_o l_c^2 H_o}{\ln(2n) - 1}. \tag{42}$$

Substituting n by equation 41, we can calculate the flux for the given length to diameter ratio and place it on the normalized flux graph. Since this method deals with fundamental units, it is used in the optimization instead of the previous model based on equation 5.

This approach also has the advantage of helping choose a wire distribution. It was previously explained that the flux has a triangular distribution along the core. The amount of flux which threads a certain portion of the core is described by equation 33. This equation can be modified to be written in terms of length to diameter ratio such that

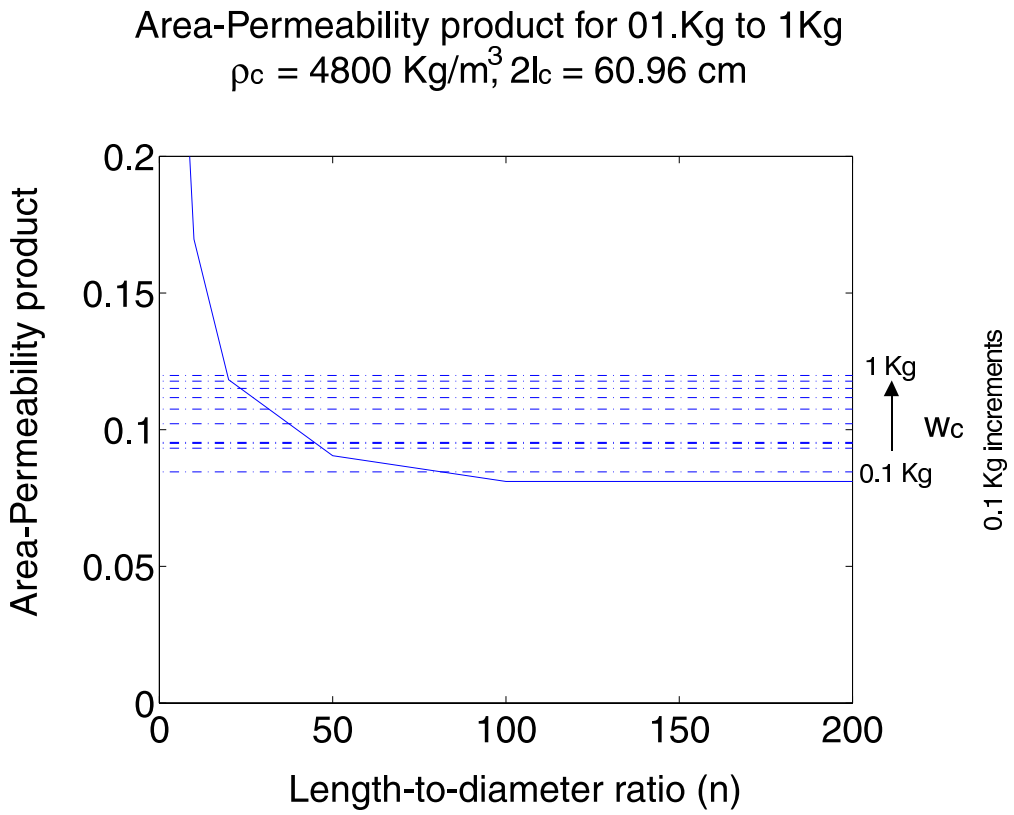

Figure 16: Area-Permeability product for given weight.

$$\phi_c = \left(\frac{\pi \mu_o l_c^2 H_o}{\ln(2n) - 1}\right)\left(1 - \frac{s_1}{2l_c}\right). \tag{43}$$

From equation 43, it is expected that short cores which are centered around the middle of the core would yield higher levels of flux. This assumption is verified in figure 17.

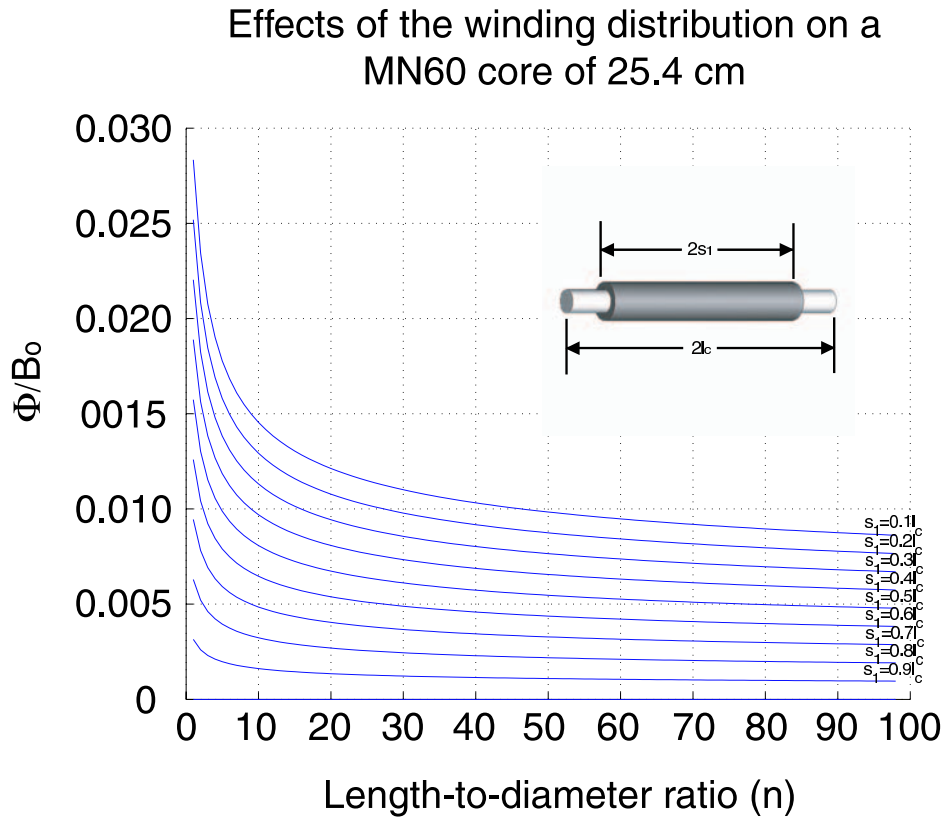

Figure 17: Effects of winding distribution for a (MN60) core of length 25.4 cm.

Thus a coil which is short in comparison to the length of the core will have more flux passing through it than if it is distributed over a longer part of the core. This however does not guarantee the magnetometer with the highest signal-to-noise ratio (SNR). Recall that

the output voltage is determined by the number of turns multiplied by the time derivative of the flux which passes through the winding. When a short coil is constructed around the center of the core, and a large number of turns is required, the radius of the turn increases rapidly. This means that more copper is required to make the same amount of turns which makes the winding heavier and the increased wire length also makes the resistance higher. A higher resistance in turns gives a higher amount of thermal noise, and thus the gains obtained by wrapping the center of the core may not be realized in practice.

In order to investigate this possibility, a numerical model was developed. A MATLAB® program was written to determine the optimal wire distribution for a set weight of copper. The first step of the calculations was to determine the length of wire that was possible given the gauge and the density of the wire. This is done by using equation 9. From this information, the resistance of the wire is calculated using equation 22. The length of wire is then spooled on the core, following the method described in section 6.1. Once the wire is completely spooled, the program knows the exact number of turns and thus the output signal that can be achieved and the resistance of the winding from which it computes the noise. Figure 18 illustrate the results for various wire gauges.

From these results, the optimal distribution of the winding is between 60% and 70 % of the length of the core.

8.1 Core Optimization

The set of curves presented in Section 8 helps to illustrate the impact of the dimensions of the core on the performance of the CIM. In order to illustrate the effectiveness of these curves, a test case is presented below.

Assume that a CIM has a core with a length of 25.4 cm. The core is made of MN60,

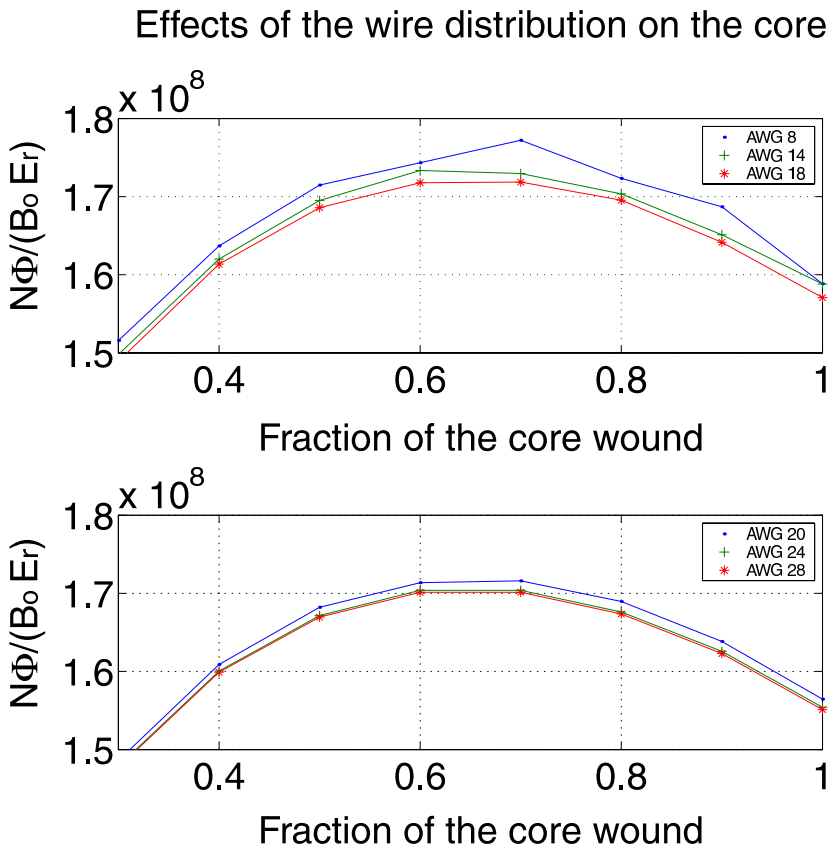

Figure 18: Dependence of the SNR on wire distribution

which has a density of 4800 Kg/m^3. Figure 19 illustrates the normalized flux graph for varying length to diameter ratios n.

For $0.1 \leq W_c \leq 1.0$Kg, n will span between approximately 5 and 22. What if the core length is increased by 2.4 times to 60.96 cm ? The results are seen in figure 19.

The range of the weight still spans from 0.1 Kg to 1Kg, but the length to diameter ratio is now between 25 and 92. For this weight class, we are operating on a lower region of the normalized flux graph, but all the curves have been pushed upward to higher normalized flux values. In fact, all the values are about 4 times greater than they were when the core was 25.4 cm. This means that the core can be made lighter and still outperform the heavier core. For example, a core which has a weight of 0.4 Kg and a length of 60.96 cm will have a normalized flux 3.6 times greater than a core of 0.8 Kg at 25.4 cm. The advantage of operating on the lower part of the normalized flux graph is that a decrease in weight does not severely impact the normalized flux. This means that the flux in the core of 0.2 Kg, and a length of 60.96 cm will only be 7 % less than in a core twice this weight at the same length. This also means that a core which is 4 times lighter at 60.96 cm can still outperform the heavier core by 3.3 times. At this point, it is important to note that the maximum length to diameter ratio that can be used depends on the initial permeability of the core material. As the core gets longer, we must start using materials with higher initial permeability in order to see the benefits predicted otherwise the apparent permeability becomes limited by the intial permeability of the material. Figure 9 should be used to determine the initial permeability of the material necessary to geometry limit the design.

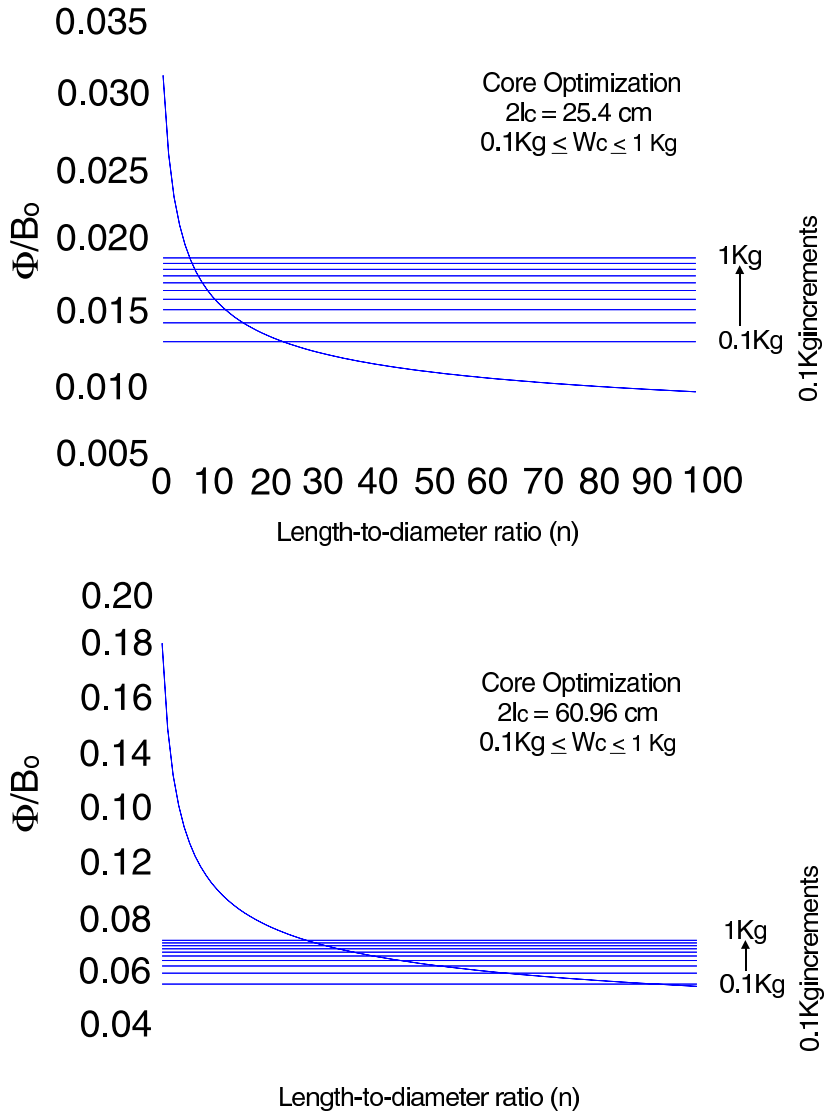

Figure 19: Comparison of two permeable cores with different length-to-diameter ratios

9 Array Concept

In ATEM, the length of the CIM is limited by the allowable dimensions of the rectangular parallelepiped[1] in which the three axis CIM can be mounted. This places an upper limit on the length of the CIM and fixes one of the dimensions in the optimization problem. A decrease in the core diameter will increase the apparent permeability but will decrease the area of the core as seen in section 8. As seen in section 8.1, slender cores will be lighter and will have higher permeability than stout cores but unfortunately, they will also have less area.

The decrease in area is a significant obstacle in increasing the overall sensitivity of the CIM. Since slender cores are lighter than stout cores, for equal weight we can have multiple slender cores. The Single Axis Induction Magnetometer Array (SAIMA) idea is to use multiple Elemental Induction Magnetometers (EIM)s in order to increase the area and permeability while maintaining the same weight as a Conventional Induction Magnetometer (CIM). A SAIMA combines high permeability and large total area which sums up to a higher amount of flux being channeled through the windings and larger overall sensitivity. The induced voltages can be combined in series for a higher voltage, or in parallel for a higher current.

The increase in sensitivity is not the only advantage of the SAIMA. Because the winding is distributed on multiple EIMs the overall length of wire used in the winding is reduced and the individual number of turns per EIM is also reduced. Since the overall number of turns remain constant, but the thermal noise attributed to the winding resistance is decreased, the SNR is increased. Less wire also means less weight and thus, a SAIMA can use heavier gauge wire reducing even further the thermal noise of the SAIMA. Another

[1] Term used to define rectangular box [Peterson60]

notable advantage of the distributed winding of the SAIMA is the decrease in inductance. The inductance of the EIMs add in series thus the inductance grows linearly with the addition of EIMs to the SAIMA. In comparison, the inductance of a CIM increases by the square of the number of turns. The reduced inductance is very important. The reader will remember that the impedance of an induction magnetometer plays a major role in the noise in the overall instrumentation noise observed.

9.1 Implementation

The construction of EIMs is similar to that of CIMs. The way in which they differ is in the distribution of the weight. CIMs have a unique core onto which the winding is wound. EIMs are built with cores which weigh a fraction of the core used in CIMs see figure 20 and figure 21.

The reduction in weight is due to a decrease in the diameter of the core, not of its length. This causes the area of the core to decrease. Since EIMs are lighter than CIMs, multiple EIMs can replace a single CIM. The multiple EIMs are assembled into a SAIMA. The weight of the SAIMA is equivalent to the weight of the CIM. The individual EIMs have higher apparent permeability than the original CIM and their combined cross sectional area is comparable to the area of the original CIM thus making a SAIMA more sensitive for the same total core weight.

In a SAIMA the weight of the winding is distributed among the EIMs. The smaller cross section of the EIMs, means that less copper is necessary for each turn and thus less copper is needed to obtain the same number of turns. One should remember that the number of turns is proportional to the output voltage. If the number of turns remains constant, but is divided among multiple cores, the combined weight of the winding of the EIMs will be

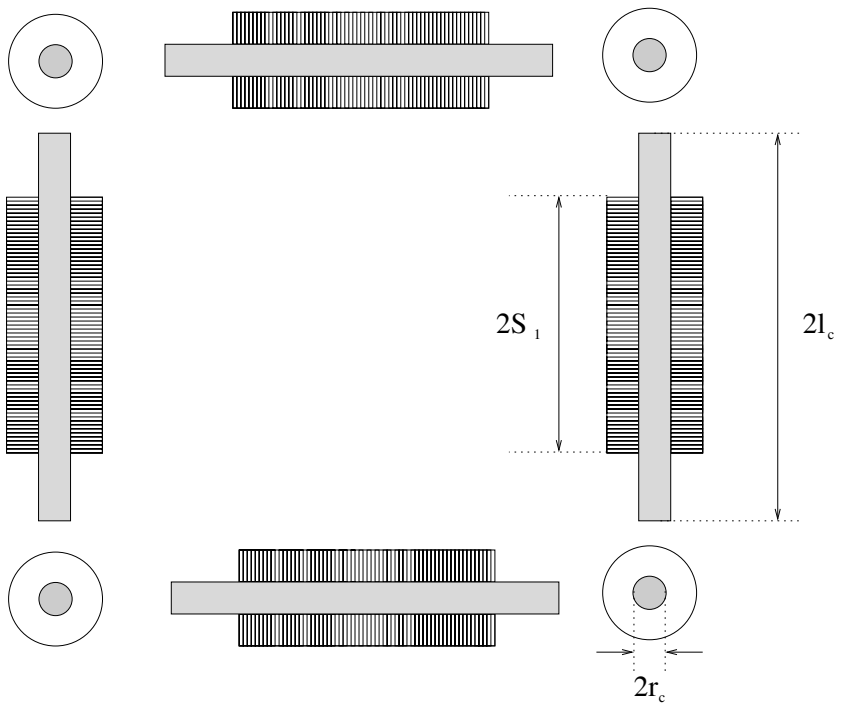

Figure 20: Cross-section of an OIMA

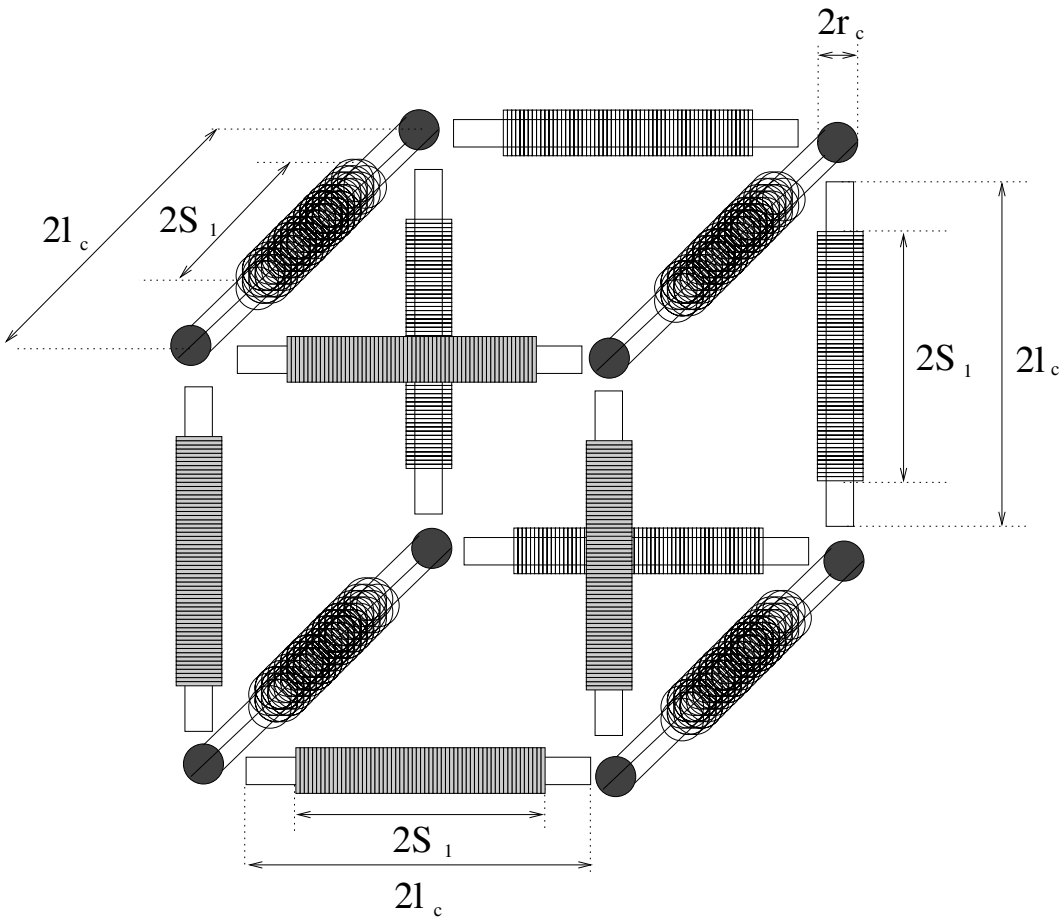

Figure 21: 3-D model of an OIMA

less than that of a CIM thus the diameter of wire used in the winding can be increased. As noted previously, this will cause the impedance of a SAIMA to be lower than an equivalent CIM and thus provide less noise. The SAIMA therefore benefits from improved sensitivity and a reduction in noise thus increasing the overall SNR further.

The distribution of the winding onto multiple EIMs also has significant implications with regards to the bandwidth of the sensor system. The CIMs are usually built with a permeable core onto which several thousand turns of wire are wound. This causes the inductance of the CIM to be very large. Since the EIMs only have a fraction of the total winding, their inductance is much smaller than that of the CIM. When the EIMs are spaced properly, their mutual inductance is minimal and thus the total inductance of the SAIMA is the simple algebraic sum of inductance of the respective EIMs. Closer spacing causes mutual inductance and thus the inductance is higher than would be expected by simple algebraic sum. If the spacing is increased, the volume needed to house the structure becomes cumbersome. The minimum spacing to limit the mutual inductance of the EIM was found through simulations, using Microwave Studio©. These simulations revealed that parallel EIMs should be spaced one core length from each other. The smaller inductance for the SAIMA means that it will self resonate at higher frequencies thus allowing larger bandwidths.

New methods of vibration noise suppression require that the magnetic field of interest be resolved into three orthogonal quantities [Munkholm97]. The additional information provided by these quantities also provides further information to the geophysicist in order to characterize the buried structures. For these reasons, the Orthogonal Conventional Induction Magnetometer (OCIM) has gained much popularity in ATEM. Since a SAIMA provides advantages over a CIM, it is logical to replace the three CIMs of the OCIM by

three SAIMAs thus creating an Orthogonal Induction Magnetometer Array (OIMA). The OIMA retains the advantages of the individual SAIMAs while occupying the same volume of the rectangular parallelepiped containing the OCIM.

10 Calibration

In order to calibrate a CIM it is necessary to have a known magnetic field. The methods used to generate this known magnetic field can vary greatly. The methods covered in the following subsections aim at providing a known magnetic field to excite a signal in the induction magnetometer. The overall performance of the CIM such as its frequency response and its sensitivity can be evaluated by using these methods.

10.1 Magnetic Field Sources

10.1.1 TEM (Transverse ElectroMagnetic) Line

This apparatus is based on the theory of parallel plate waveguides and is usually used to generate a known electric field. The parallel plate waveguides can propagate TEM, TM and TE modes. In this case we are only interested in the TEM mode as it is the one which will exist in the frequency band of interest. The TEM line is built by separating two conducting plates by a distance d. Figure 22 illustrates the geometry of the TEM line.

According to Pozar [Pozar98] , the impedance of the line for the TEM mode is given by

$$Z_{TEM} = \frac{\eta d}{w}. \tag{44}$$

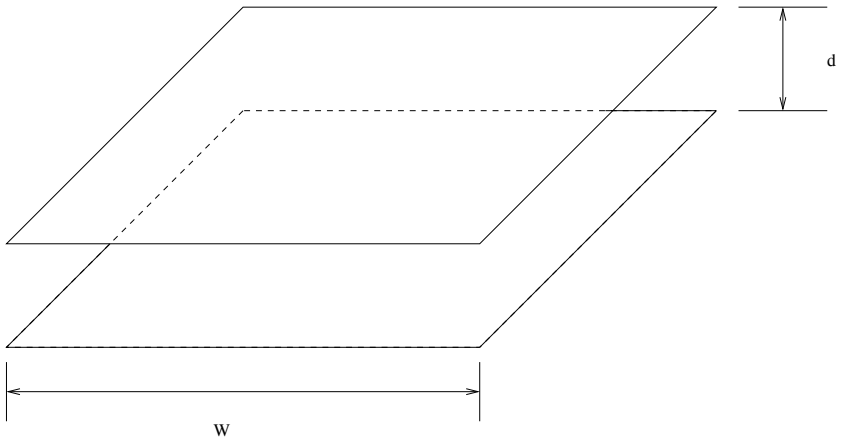

Figure 22: Geometry of Transverse ElectroMagnetic line

where $\eta = \sqrt{\mu/\varepsilon}$ is the intrinsic impedance of the medium between the plates, d is the distance which separates the plates and w is the width of the plates. In the case of the TEM line, the medium which fills the space between the plates is air, thus $\eta = \sqrt{\mu_o/\varepsilon_o} \backsimeq 377\Omega$. In order to feed at TEM line correctly it is important to ensure that the input impedance matches that of the source. This is why TEM lines are usually fitted with tapered sections on each end. These act as impedance transformers which match the Z_{TEM} to the characteristic impedance of the source. According to Pozar [Pozar98], the electric and magnetic fields present in the TEM line for the TEM mode are described by the following

$$\begin{aligned} E_z &= 0 \\ H_z &= 0 \\ E_x &= 0 \\ E_y &= \left(\tfrac{-V_o}{d}\right) e^{-j\beta z} \\ H_x &= \left(\tfrac{V_o}{\eta d}\right) e^{-j\beta z} \\ H_y &= 0\,, \end{aligned} \tag{45}$$

where V_o is the voltage difference on the plates, d is the distance that separate the plates, β is the propagation constant between the plates, η is the intrinsic impedance of air and z is the position along the TEM line. Again, since air is between the plates, $\beta = \omega\sqrt{\mu_o \varepsilon_o}$, where ω is the frequency of the signal in radiants per seconds. Because of the frequencies at which the TEM line is to be used and its short length, $e^{-j\beta z} \backsimeq 1$, which means that the equations for E_y and H_x can be simplified to

$$\begin{aligned} E_y &\backsimeq \tfrac{-Vo}{d} \\ H_x &\backsimeq \tfrac{V_o}{\eta d} \end{aligned} \quad . \tag{46}$$

In this case, the disadvantage with this method of generating a known magnetic field is that these equations are only true for positions well within the area of the parallel plates. Fringing occurs at the edge of the plates which causes the fields to differ from the value described by equation 46. The dimensions of the TEM line available were not sufficient to assure a known uniform test field for calibrating a CIM of 60.96 cm. Given the expense and the size of the TEM line that would need to be constructed to test large CIMs, this calibration method was not pursued.

10.1.2 Helmholtz Coils

These pairs of coils are often used when a uniform magnetic field is necessary. The coils are spaced one radius away from each other. The current is applied in the same direction onto both coils, this generates the magnetic field. The geometry of the Helmholtz coils is illustrated in Figure 23.

The gradient of the magnetic field goes to zero at the center of the Helmholtz coil pair. The magnetic field at the center of the Helmholtz coils is

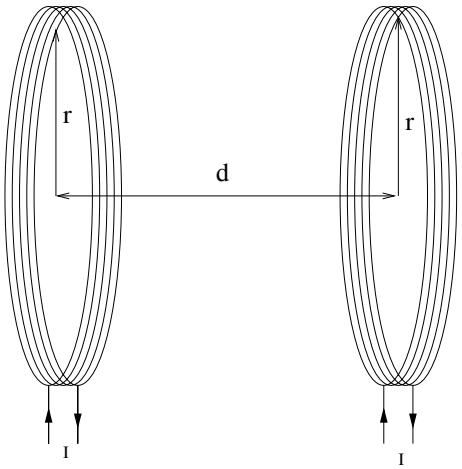

Figure 23: Helmholtz coils

$$H_x = \frac{N I r^2}{\left(\frac{d}{2}^2 + r^2\right)^{\frac{3}{2}}}, \tag{47}$$

where r is the radius of the coils, d is the spacing between the coils and I is the current applied to the coils. The reader should remember that $d = r$ in the case of the Helmholtz coils.

These Helmholtz coils were not used for the calibration of the induction magnetometer because their size would have been too imposing. The smallest Helmholtz coils that would accommodate the induction magnetometers being designed would have had a diameter of at least 1.4 m. Also, in order to ensure that the effects due to the proximity of the ends of the induction magnetometer to the Helmholtz coils was not significant, the coils would have been scaled up to a diameter of approximately 2 m. The size of this setup would not allow easy transport to remote sites in order to make low level measurements, thus this option was not pursued.

10.1.3 Infinite Solenoid

An infinite solenoid has an axial magnetic field described by

$$H_x = \frac{NI}{2\sqrt{r^2 + l^2}}. \tag{48}$$

where N is the number of turns, I is the current, r is the radius of the solenoid and l is the length. Although an infinite solenoid is not achievable in practice, if the length is sufficiently large in comparison to the radius, the field in the middle of the solenoid will be uniform and described by equation 48. In practice, it was found that when the length of the solenoid is ten times the radius, the field was sufficiently uniform for calibration purpose. This method for calibration was used to calibrate CIMs which had low permeability cores, but unfortunately it could not be used for EIMs equipped with higher permeability cores. The mutual inductance between the solenoid and the EIM under test caused the solenoid to self-resonate in the band of interest. This resonance complicated the measurements since the current and hence the magnetic field in the solenoid varied with frequency.

10.1.4 Transmitting Loop

This method of calibration resembles most the way in which the CIM is to be used. Since the frequencies in use are very low, their wavelengths are of gigantic proportions measuring several Mm. These long wavelengths mean that the induction magnetometer will be in the near field region of both the primary field from the transmitter and the secondary field from the conductive target. Although the magnetic field is varying with time, it can be modeled accurately by a static magnetic field. According to Telford *et al* [Telford90], if the transmitter loop and the receiver loops are coplanar and separated by at least seven times the radius of the transmitter loop, the field strength at a distance R is well approximated by

$$H_z = -\frac{INA}{4\pi R^3}, \tag{49}$$

where I is the current in the loop, N is the number of turns in the transmitter loop, A is the area of the transmitter loop, R is the distance at which the field is to be measured. In order to obtain accurate calibration with this method, the alignment of the induction magnetometer and the transmitter must be perfect and the distance between the two must be known accurately. Care should also be taken to limit the amount of conductors and permeable materials placed in the vicinity of the test setup since they will distort the field and lead to improper calibration.

10.2 Instrumentation

10.2.1 Sensitivity and Frequency Response Measurements

Once the proper magnetic field source is chosen, it must be fed the excitation signal. Most of the sources considered have been continuous wave sources. Among them, is the HP signal wave analyzer HP3581A. This instrument allows the frequency source to be swept over the band of interest while the bandpass filter at the receiver tracks it in frequency. This instrument makes it possible to make measurements in noisy environments since its narrow band input filter rejects the noise which is outside the band. Unfortunately, due to the age of the HP3581A, it is not equipped with a convenient data acquisition system. A Tektronix oscilloscope, the TDS210, had to be programmed to acquire the voltages from the x-y plotter terminals of the HP3581A and transfer them to a computer for storage. The routines were written in MATLAB® and the TDS210 was connected to a laptop computer via a parallel port for the control of the scope and the data transfer. This setup permits

the frequency response and the sensitivity of the induction magnetometer under test to be determined.

The calibration is done by subjecting the induction magnetometer to a known magnetic field. The voltage at the terminals of the induction magnetometer is recorded using the HP3581A and the data acquisition system. The frequency information is also recorded by the system. At the end of a sweep, the frequency response of the CIM for the band of interest is known. The current in the structure that generates the known magnetic field is monitored during the sweep in order to ensure that the field remains constant over the band. With this information it is possible to compute the sensitivity of the CIM over the band. The known magnetic field is simply divided by the voltage measured during the sweep. In order to ensure that the results are accurate, the experiment should be done a second time, but this time the magnetic field intensity should be different than in the first case. This method also constitute a limited test for linearity. From the voltage at the terminals of the CIM, one should be able to compute the magnetic field to which it is subjected. From this information the current in the exciting structure can be calculated. If this current value is the same as the one measured, the induction magnetometer is properly calibrated and ready for use.

A transient source can also be used in order to verify the operation of the CIM. This source mimics best the behavior of the CIM when it is used in the exploration system. This type of source makes it possible to observe any instability that may be present in the CIM because of self resonance. The transient source is built by making a tank circuit resonate. Silicon Control Rectifiers are used to switch power to the transmitter loop and the capacitor bank. The design of this transmitter will not be discussed further in this document.

11 Construction of an Induction Magnetometer

High permeability cores are not easily acquired. The types of ferrites or permeable alloys that compose the cores of the CIMs are not usually available as a standard product and thus must be specially ordered from the manufacturers. Even then, the dimensions available are governed by physical properties of the material and the tooling available. Even if an optimal design can be found in theory, it may not be affordable to pursue it in practice given the limitations of the tooling. The CIMs developed during this work were subject to these limitations.

MN60 was selected as the permeable material for the core of the induction magnetometer. It is a ferrite made from iron, manganese and zinc. This ferrite had the appearance of a dark ceramic material and was very brittle. The initial permeability of MN60 was 6500, it had a dc-volume resistivity of 200 ohms - cm and it had a density of 4.3 g/cm^3. Other materials such as HYMU80 were considered for the construction of the core. This zinc alloy had a very high initial permeability which was affected by the annealing process. Initial permeabilities often reached in excess of 100 000. This initial permeability was much higher than was required for a geometry limited induction magnetometer and thus this exotic material was of little use in this application. HYMU80 was also heavier than MN60 and had lower resistivity which caused eddy current problems if the laminations were not thin enough.

The MN60 ferrite was acquired in the form of rods. Each rod had a diameter of 5/8 of an inch and were 8 inches long. Three of these rods were glued together with epoxy in order to obtain a core measuring 24 inches. The length-to-diameter ratio of the resulting core was therefore 38.4. The core could be made lighter by reducing the diameter of the core, however due to the brittle nature of the MN60 ferrite, the CIM would be too fragile

to be used in the field. The core was placed in a lathe equipped with a counting mechanism and copper wire was spun onto the central 60 % of the core as suggested by section 8.

12 Validation of Concepts

The mathematical representation which describes the physical and electrical parameters of a CIM were developed in section 6. Experiments were performed in order to verify the accuracy of the model. Each of these experiments are described below along with their results.

12.1 Wooden Core Standard

In order to validate the physical model of the CIM, a wooden core with the same dimensions as our expected permeable core was built. This core allowed verification of the model predicting the weight and the resistance of a scramble wound coil for a set number of turns and wire gauge as described in sections 6.1 and 6.2. From prior experimentation with coil winding, it was discovered that the method used to scramble wind a coil by Custom Research filled about 25 % of a layer before proceeding to the next one. This filling factor along with the diameter of the core, the length of the section to be wound, and the wire gauge were entered in the model. The MATLAB ® routine returned the number of turns achievable, the resistance of the coil and the expected weight of copper. In the experiment, 2025 turns were spun onto the wooden core. The expected weight calculated by the model for this coil was 0.170 Kg, and the measured weight was 0.174 Kg for a percentage difference of about 2.3 %. The expected resistance by the model for this coil was 19.5 Ω and the measured resistance was 20.3 Ω when measured with digital multimeter,

for a percentage difference of about 4 %. This procedure was repeated several times and the results remained as predicted by the model.

The self-capacitance present in the induction magnetometer was also determined during this experiment. The measured inductance L and the resonant frequency f_o were placed into equation 25. This equation was then manipulated in order to isolate the capacitance of the circuit. Interestingly enough, the value of the capacitance remained around 300 pF once 1000 turns were spooled onto the core. Due to the nature of the winding technique, there does not exist a mathematical model which predicts the capacitance of the coil. During subsequent experiments described in section 12.2 the calculated capacitance remained close to 300 pF and this even if 4000 turns were spooled onto a ferrite core.

12.2 Ferrite Core CIM

The second step in validating the model proposed in section 6.2 was to investigate its ability in predicting the self-inductance and the induced voltage in the induction magnetometer. The measurements were conducted inside an anechoic chamber. The chamber did not offer any protection from noisy magnetic fields but did shield appropriately from electric field noise observed outside the chamber. The inductance was measured by using an electronic RLC bridge at 1 kHz. The induced voltage was measured by using an oscilloscope. The source used to generate the magnetic field for this experiment was a small transmitter loop constructed of 28 turns of copper magnet wire around a Pyrex petri dish with a diameter of 9.4 cm. The following diagram illustrates the test setup used.

A variable resistor was used as the *compensation circuit* during this experiment. In order to determine its value, an excitation coil was wrapped around the CIM. A 1 kHz triangular wave was applied to the exciting coil. The reader will recall that the voltage

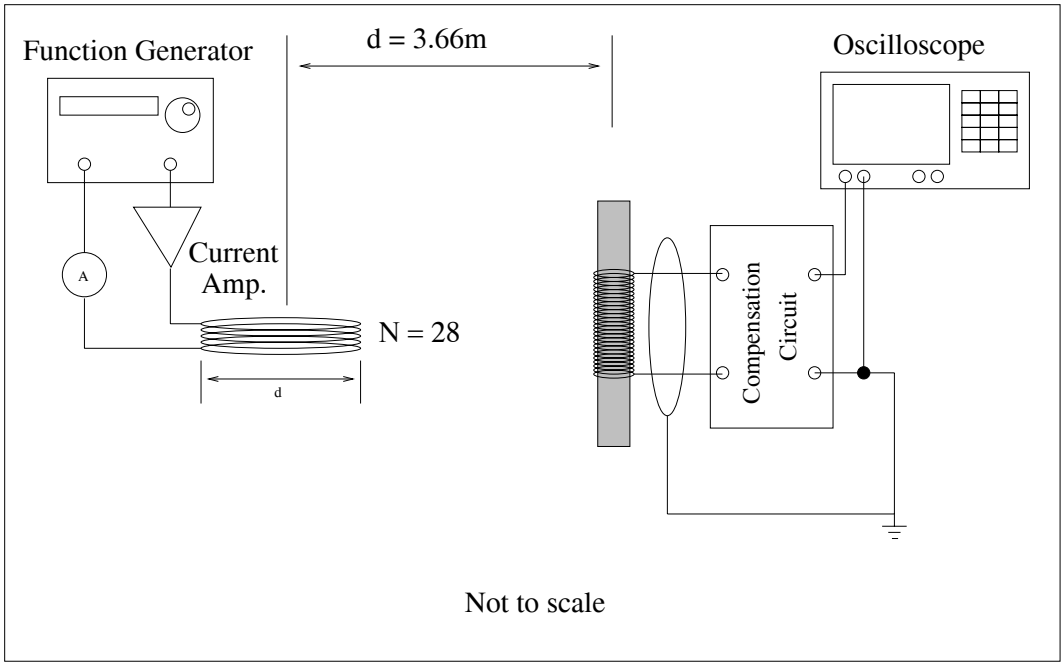

Figure 24: Experimental setup to verify induced voltage in induction magnetometer

induced in a CIM was proportional to the time derivate of the flux, thus a square wave voltage was expected at the terminals of the CIM. When the CIM is not properly damped, the square wave has high levels of overshoot. The resistance value was adjusted to 38.23 kΩ at which point the frequency response of the CIM was critically damped. The current in the transmitter loop was monitored with a digital multimeter. The first trials yielded induced voltages scaled by a factor of two over what was predicted by theory. After investigation, it was determined that the assumptions made by Telford *et al.* [Telford90] did not hold for the original test setup. Equation 49 assumes that the transmitter and the receiver are coplanar. Given the size of the CIM in comparison with the transmitter, seven times the radius of the transmitter was not sufficent to limit mutual coupling. The test setup was modified, and the spacing between the transmitter and the CIM was increased to 3.66m. A

function generator was used to generate a continuous sine wave of 1 kHz. At this distance, the small transmitter loop and the function generator could no longer generate a suitable field for detection. A current amplifier was introduced in the circuit. The current was controlled during the experiment and remained at 1A while the frequency was swept. The field strength at the receiver was calculated to be 0.4nT. It was estimated that about 4140 turns were spooled onto the induction magnetometer. The expected inductance for this distribution of winding using equation 30, from the work of Kaplan *et al.* [Kaplan02] was 3.250 H. The inductance measured was 3.258 H for a percentage difference of 0.2 %. For the same number of turns, equation 27, which assumes an infinite solenoid, predicted an inductance of 3.7626 H which differed by 15.4 % with respect to the measured value.

Figure 25 illustrates the expected voltage across R_p versus the measured value. One can see that the measured results approached what was predicted from theory. It is expected that as the distance increases, the voltage seen across R_p will tend to the voltage predicted by equation 34. The discreptency between the voltages calculated and the ones measured were all within 25 %.

12.3 Array Concept

A similar experiment was conducted in order to validate the array concept. Figure 26 illustrates the setup used during the experiment. The two CIMs were connected in series and compensated with an adjustable resistor set to 89.5 kΩ. The transmitter loop was positioned between the two CIMs. The distance between the transmitter coil and the CIMs was 61 cm. The current was adjusted and controlled during the experiment to remain at 51.3 mA as was done in section 12.2. The frequency of the source was varied from 100 Hz to 20 kHz. The voltages measured and the improvements observed are illustrated in Fig-

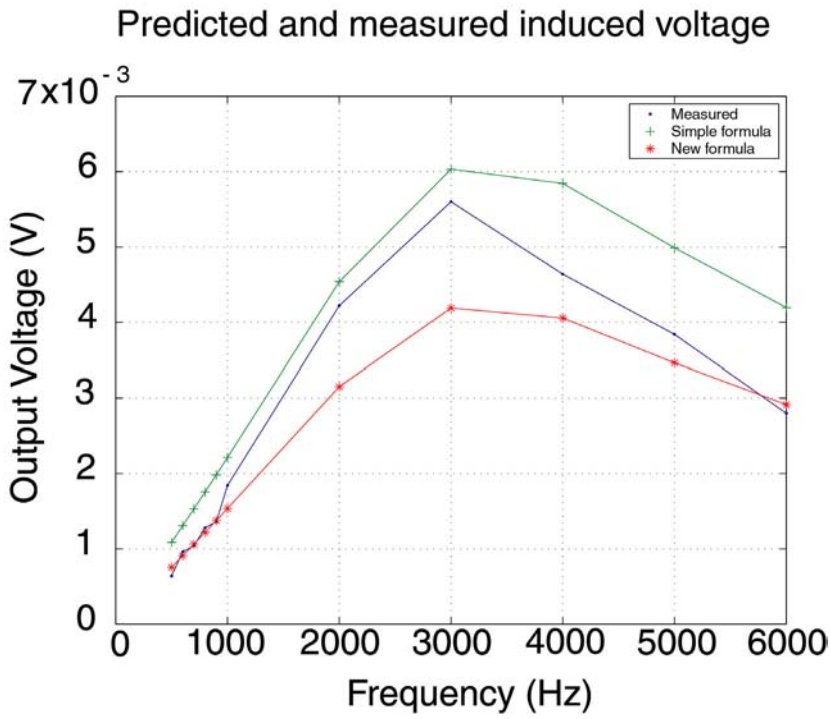

Figure 25: Comparison of expected and measured voltage for a CIM. New formula is equation 30 and simple formula is equation 27.

ure 27. The results were as expected yielding a voltage gain of approximately 6 dB. Given the limited accuracy of the measurement system, these results indicate that the concept of the array works.

12.4 Compensation Circuit

The I-to-V conversion circuit proposed by Hauser [Hauser90] and Macintyre [Macintyre80] was constructed. A Sallen & Key low-pass filter with a 20 kHz cutoff was added in order to provide a low pass frequency characteristic. The schematic used can be found in figure 28. PSPICE was used to simulate the output voltage noise of the I-to-V converter and the parallel resistor compensation. The results are found in Figure 29.

The reader will remember that large resistor values R_f can be used in the I-to-V converter circuit without adding significant noise. This circuit provides greater stability when compared with a simple parallel resistor. Figure 30 illustrates the frequency response of two CIMs connected to this compensation circuit. The frequency response of the CIM and the compensation circuit does not demonstrate any resonant behaviour. The same figure also shows the frequency response of the two CIMs when compensated with R_p. These results show that there are significant advantages in using the new compensation circuit as opposed to using the simple parallel resistor option.

13 Conclusions

This document provides a comprehensive design procedure and optimization method for induction magnetometers to be used in ATEM. These optimizations have led to the development of a novel idea for the implementation of induction magnetometers. For similar

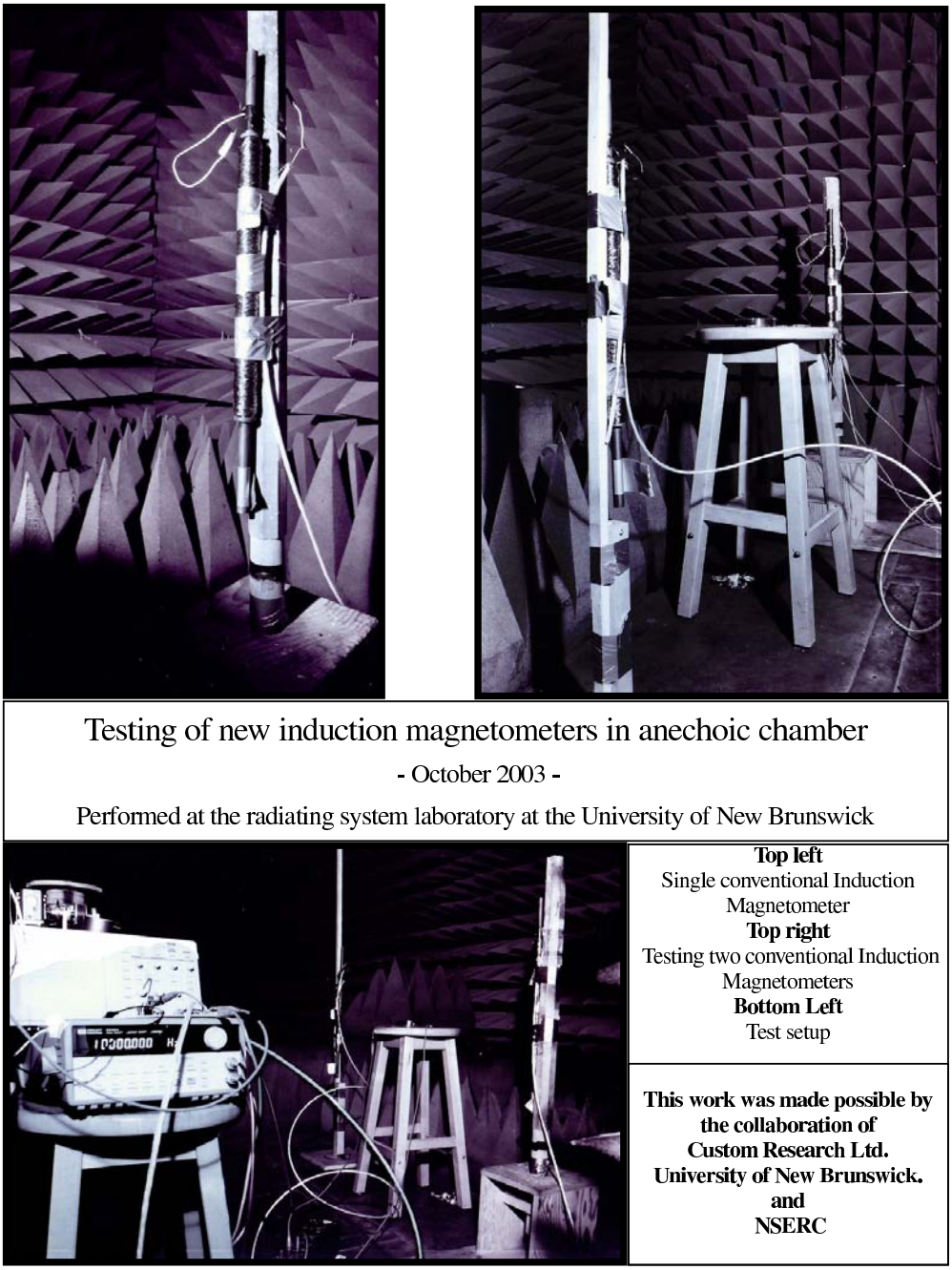

Figure 26: Experimental setup used during the verification of the array concept

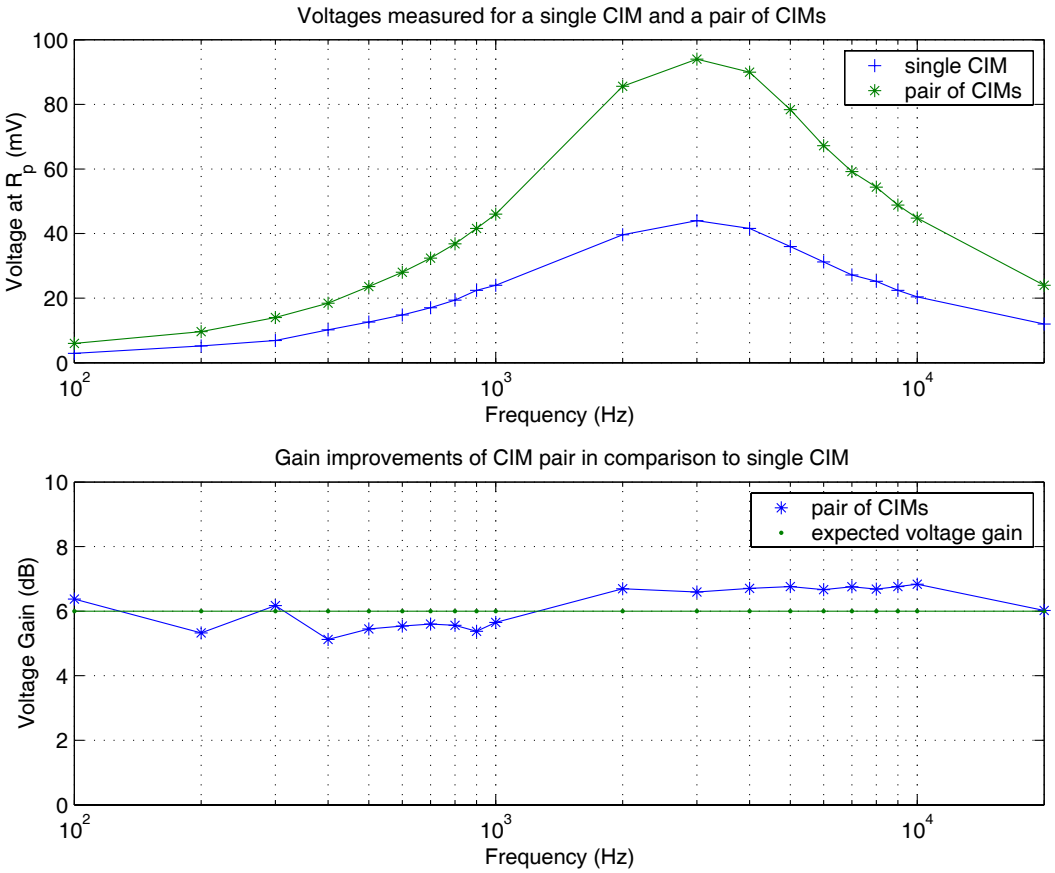

Figure 27: Voltage increase due to the addition of a second CIM

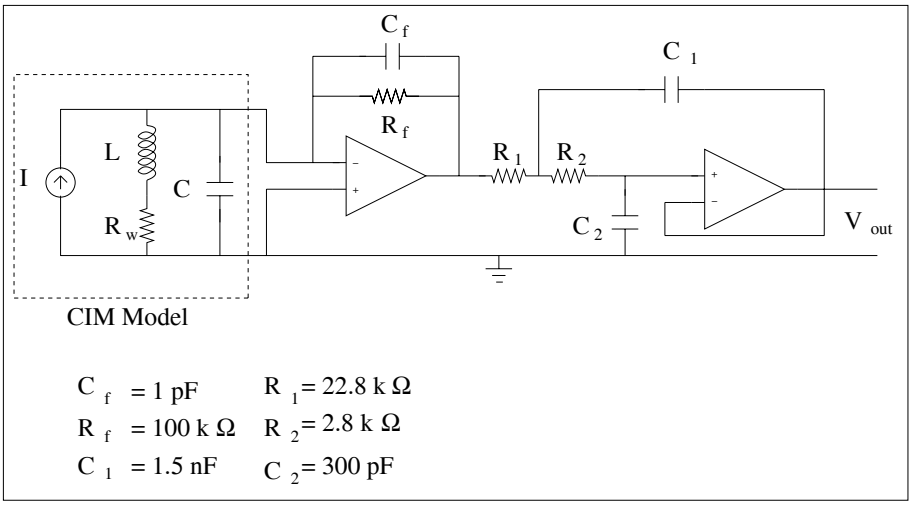

Figure 28: I-to-V compensation circuit and Sallen & Key low pass filter

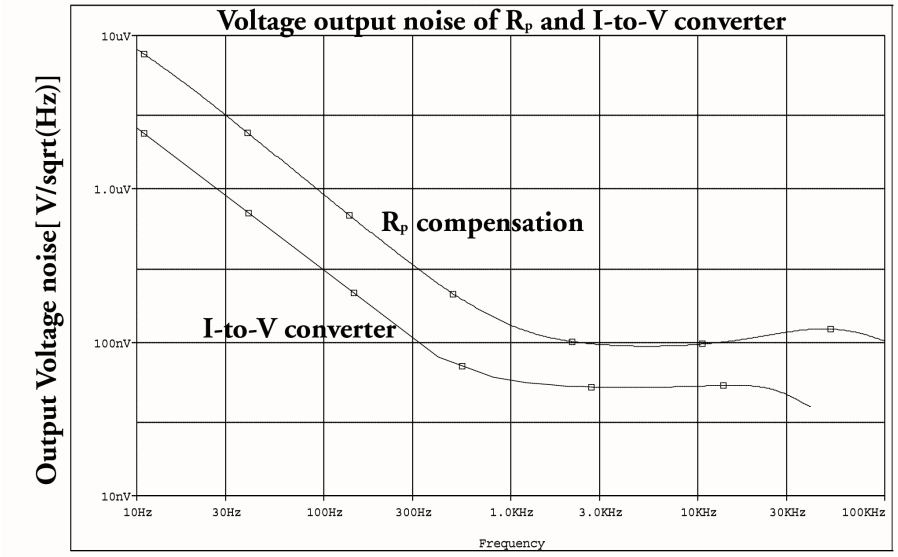

Figure 29: Voltage output noise of the two different compensation circuits

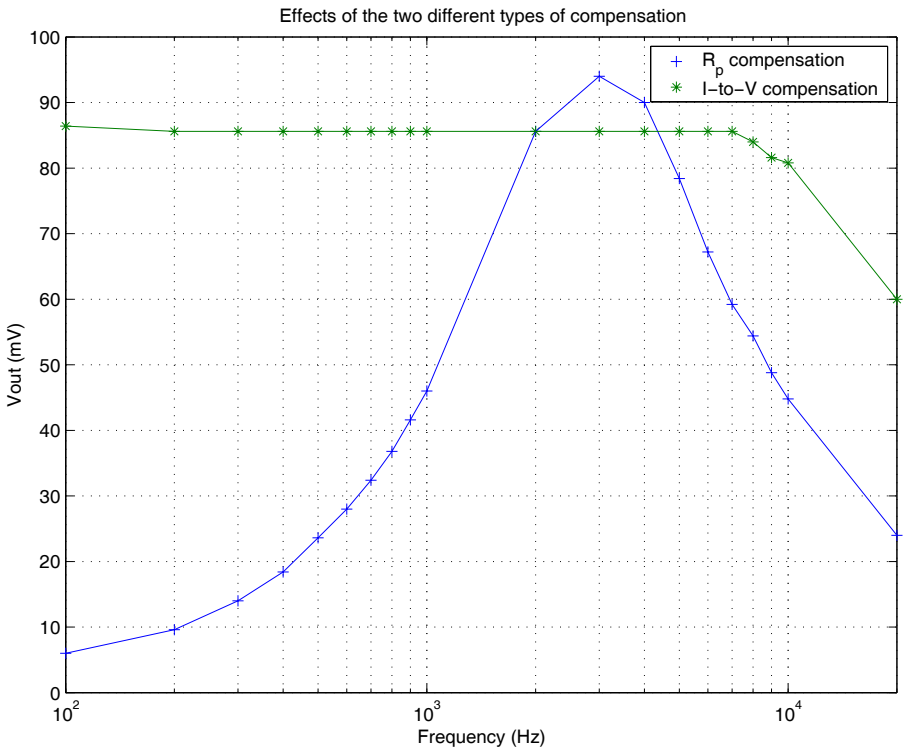

Figure 30: Comparison of the two different compensation methods

weight, it was shown that multiple smaller coils could be constructed and placed into an array. The SAIMA provides a larger amount of signal while the decrease in thermal noise and in inductance reduce the noise of the sensor system. The measurements done in order to verify the theory developed in this thesis were all successful. The inductance calculations and the measurements agreed within 0.2 %, the expected winding weight agreed within 2.3 % and the DC resistance was within 4 %. The induced voltage during the transmitting loop calibration test was underestimated by equation 34 while it was overestimated by equation 5. The predicted and measured values were all observed to be within 25 %. The three greatest sources of errors associated with this measurement were, the distance between the transmitter and the receiver, the possible presence of magnetic materials and the poor calibration of the ammeter. As discussed in section 12.2, the distance to the transmitter was not sufficient to eliminate the mutual coupling between the transmitter and the CIM. The distance measurements were also made with a tape measure, from the estimated center from each device. This measurement method only allowed accuracy to approximately 1 cm introducing uncertainty in the field strength at the position where the CIM was mounted. The anechoic chamber provided good shielding from electrical noise, but the antenna positioner in the chamber may have distorted the magnetic field from the transmitter and thus changed the nature of the field seen at the receiver. The test setup, transmitter and receiver, were always placed at the same distance from the positioner. Finally, it was impossible to obtain a calibration certificate for the ammeter used during the experiment. Errors in the measurement of the current directly impact the field strength produced at the transmitter. Overall, this project was a success, and the product developed during this work may be implemented in the ATEM system developed by Custom Research Ltd.

14 Future Work

The final construction of the OIMA is still pending. Construction of the support structure and suspension system is almost completed. Once completed , the operation of the OIMA may be verified in the Radiating Systems Research lab at UNB and on the ground far away from civilization. Once this testing is done, the OIMA will be tested in flight aboard the new ATEM system developed by Custom Research.

References

[CDtechnologies] "Inductors", Application Notes, 1400 Union Meeting Road, P.O. Box 3053 Blue Bell, PA 19422. MPAN-01 last accessed April 2003, 2003.

[Becker67] A. Becker, "Design formulas for electromagnetic sensing coils", *Geoexploration*, pp. 81–88, January 1967.

[Boylestad94] R. L. Boylestad, *Introductory Circuit Analysis*, Toronto, Ontario, Canada: Maxwell Macmillan Canada, seventh ed., 1994.

[Bozorth93] R. M. Bozorth, *Ferromagnetism*, New York, New York, United States of America: IEEE Press, 1993.

[Bozorth42] R. M. Bozorth and D. M. Chapin, "Demagnetizing factors of rods", *Journal of Applied Physics*, vol. 13, pp. 320–326, May 1942.

[Breen64] A. Breen, "Principles in designing instruments for electromagnetic ore prospecting", *Geoexploration*, pp. 159–168, 1964.

[Burrows78] M. L. Burrows, *ELF Communications Antennas*, Southgate House, Stevenage, Herts, England: Peter Peregrinus LTD., 1978.

[Buselli96] G. Buselli and M. Cameron, "Robust statistical methods for reducing sferics noise contaminating transient electromagnetic measurements", *Geophysics*, vol. 61, no. 6, pp. 1633–1646, November 1996.

[Butler03] K. E. Butler and R. D. Russell, "Cancellation of multiple harmonic noise series in geophysical records", *Geophysics*, vol. 68, no. 3, pp. 1083–1090, May-June 2003.

[Cheng89] D. K. Cheng, *Field and Waves Electromagnetics*, Toronto, Ontario, Canada: Addison-Wesley Publishing Company, 1989.

[Chwala01] A. Chwala, V. Schultze, R. Stolz, J. Ramos, R. IJsselsteijn, H.-G. Meyer, and D. Kretzschmar, "An HTS DC SQUID system in competition with induction coils for TEM applications", *Physica C*, , no. 354, pp. 45–48, 2001.

[Clarke89] J. Clarke, "Principles and applications of SQUIDs", *Proceedings of the IEEE*, vol. 77, no. 8, pp. 1208–1223, August 1989.

[Clem95] T. R. Clem, "Superconducting magnetic sensors operating from a moving platform", *IEEE Transactions on Applied Superconductivity*, vol. 5, no. 2, pp. 2124–2128, June 1995.

[Clem01] T. R. Clem, D. J. Overway, J. W. Purpura, J. T. Bono, R. H. Koch, J. R. Rozen, G. A. Keefe, S. Willen, and R. A. Mohling, "High-Tc SQUID Gradiometer for mobile magnetic anomaly detection", *IEEE Transactions on Applied Superconductivity*, vol. 11, no. 1, pp. 871–875, March 2001.

[Foley99] C. P. Foley, K. E. Leslie, R. Binks, C. Lewis, W. Murray, G. J. Slogett, S. Lam, B. Sankrithyan, N. Savvides, A. Katzaros, K. H. Muller, E. E. Muller, J. Pollock, J. Lee, D. L. Barrows, M. Asten, A. Maddever, G. Panjkovic, M. Downey, C. Hoffman, and R. Turner, "Field Trials using HTS SQUID Magnetometers for ground-based and airborne geophysical applications", *IEEE Transactions on Applied Superconductivity*, vol. 9, no. 2, pp. 3786–3792, June 1999.

[Foley01] C. P. Foley, K. E. Leslie, R. A. Binks, G. B. Donaldson, J. Du, S.K. Lam, P. W. Schmidt, and D. A. Clark, "Geophysical exploration using magnetic gradiometry based on HTS SQUIDs", *IEEE Transactions on Applied Superconductivity*, vol. 11, no. 1, pp. 1375–1378, March 2001.

[Frandsen69] A. M. A. Frandsen, R. E. Holzer, and E. J. Smith, "OGO Search Coil Magnetometer Experiments", *IEEE Transactions on Geoscience Electronics*, vol. GE-7, no. 2, pp. 61–68, April 1969.

[Hauser90] J. P. Hauser, "A 20Hz-to-200kHz Magnetic Flux Probe for EMI Surveys", *IEEE Transactions on Electromagnetic Compatibility*, vol. 32, no. 1, pp. 67–69, February 1990.

[Hirota00] M. Hirota, T. Furuse, K. Ebana, H. Kubo, K. Tsushima, T. Inaba, A. Shima, M. Fujinuma, and N. Tojyo, "Magnetic detection of a surface ship by an airborne LTS SQUID MAD", *IEEE Transactions on Applied Superconductivity*, vol. 11, no. 1, pp. 885–887, March 2001.

[Jaklevic64] R. C. Jaklevic, J. Lambe, A. H. Silver, and J. E. Mercereau, "Quantum interference effects in Josephson Tunneling", *Physical Review Letters*, vol. 12, no. 7, pp. 159–160, February 1964.

[Josephson62] B. D. Josephson, "Possible new effects in superconductive tunelling", *Physics Letters*, vol. 1, no. 7, pp. 251–253, July 1962.

[Green67] A. W. Green Jr. and A.A.J. Hoffman, "Micropulsation instrumentation systems at the Dallas Geomagnetic Center", *IEEE Transactions on Geoscience Electronics*, vol. GE-5, no. 1, p. 1967, March 1967.

[Kaplan94] B. Z. Kaplan, "A New Interpretation of the Relationship Existing Between Demagnetizing Factor and Inductance", *IEEE Transactions on Magnetics*, vol. 30, no. 5, pp. 2788–2794, September 1994.

[Kaplan98] B. Z. Kaplan and U. Suissa, "Treatment of extremely low frequency magnetic and electric field sensors via the rules of electromagnetic duality", *IEEE Transactions on Magnetics*, vol. 34, no. 4, pp. 2298–2305, July 1998.

[Kaplan02] B. Z. Kaplan and U. Suissa, "Evaluation of inductance for various distributions of windings on straight ferromagnetic cores: An unusual approach", *IEEE Transactions on Magnetics*, vol. 38, no. 1, pp. 246–249, January 2002.

[Kepic95] A. Kepic, *Seismoelectric Responses from Sulphide Orebodies*, Ph.D. thesis, Dept. of Geophysics and Astronomy, The University of British Columbia, September 1995.

[Lenz90] J. E. Lenz, "A Review of magnetic sensors", *Proceedings of the IEEE*, vol. 78, no. 6, pp. 973–989, June 1990.

[Lukoschus79] D. G. Lukoschus, "Optimization theory for induction-coil magnetometers at higher frequencies", *IEEE Transactions on Geoscience Eletronics*, vol. GE-17, no. 3, pp. 56–63, July 1979.

[Macintyre80] S. A. Macintyre, "A portable low noise low frequency three-axis search coil magnetometer", *IEEE Transactions on Magnetics*, vol. 16, no. 5, pp. 761–763, September 1980.

[Maxwell67] E. L. Maxwell, "Atmospheric noise from 20 Hz to 30 kHz", *Radio Science*, vol. 2, no. 6, pp. 637–644, June 1967.

[McCracken86] K. G. McCracken, M. L. Oristaglio, and G. W. Hohmann, "Minimization of noise in electromagnetic exploration systems", *Geophysics*, vol. 51, no. 3, pp. 819–832, March 1986.

[Motchenbacher93] C. D. Motchenbacher and J. A. Connelly, *Low-Noise Electronic System Design*, Toronto, Ontario, Canada: John Wiley & Sons, Inc., 1993.

[Munkholm97] M. S. Munkholm, "Motion-induced noise from vibration of a moving TEM detector coil: characterization and suppression", *Journal of Applied Geophysics*, vol. 36, pp. 21–29, January 1997.

[Nabighian88] M. N. Nabighian, *Electromagnetic Methods in Applied Geophysics*, Tulsa, Oklahoma, United States of America: Society of Exploration Geophysicists, 1988.

[Panaitov01] G. Panaitov, M. Bick, Y. Zhang, and H. J. Krause, "Effect of repetitive transmitter signals on SQUID response in geophysical TEM", *IEEE Transactions on Applied Superconductivity*, vol. 11, no. 1, pp. 888–891, March 2001.

[Parasnis97] D. S. Parasnis, *Principles of Applied Geophysics, Fifth Edition*, New York, New York, United States of America: Chapman & Hall, 1997.

[Peterson60] T. S. Peterson, *Calculus with Analytic Geometry*, New York, New York, United States of Americ: Harper & Row, Publishers, Incorporated, 1960.

[Pozar98] D. M. Pozar, *Microwave Engineering, Second Edition*, Toronto, Ontario, Canada: John Wiley & Sons, Inc., 1998.

[Randa95] J. Randa, D. Gilliland, W. Gjertson, W. Lauber, and M. McInerney, "Catalogue of electromagnetic environment measurements, 30-300 Hz", *IEEE Transactions on Electromagnetic Compatability*, vol. 37, no. 1, pp. 26–33, February 1995.

[Slemon66] G. R. Slemon, *Magnetoelectric Devices*, New York, New York, United States of America: John Wiley & Sons, Inc., 1966.

[Stewart95] J. Stewart, *Calculus: Early Transcendentals, Third Edition*, Scarborough, Ontario, Canada: Brooks/Cole Publishing Company, 1995.

[Telford90] W. M. Telford, L. P. Geldart, and R. E. Sheiff, *Applied Geophysics, Second Edition*, Cambridge, United Kingdom: Cambridge University Press, 1990.

[Watt67] A. D. Watt, *VLF Radio Engineering*, Toronto, Ontario, Canada: Pergamon Press, 1967.